



Petrogenesis of peralkaline rhyolites in an intra-plate setting: Glass House Mountains, southeast Queensland, Australia



Fengli Shao ^{a,b,*}, Yaoling Niu ^{a,b,c,*}, Marcel Regelous ^d, Di-Cheng Zhu ^b

^a Institute of Oceanology, Chinese Academy of Sciences, Qingdao 266071, China

^b School of Earth Science and Resources, China University of Geosciences, Beijing 100083, China

^c Department of Earth Sciences, Durham University, Durham DH1 3LE, UK

^d GeoZentrumNordbayern, Universität Erlangen-Nürnberg, D-91054 Erlangen, Germany

ARTICLE INFO

Article history:

Received 12 July 2014

Accepted 21 December 2014

Available online 27 December 2014

Keywords:

Peralkaline rhyolites

High Nb and Ta

Very high Sr isotope ratios

Daly Gap

Glass House Mountains

Southeast Queensland

ABSTRACT

We report petrological and geochemical data on coeval trachybasalts, syenites with enclaves, trachytes, peralkaline rhyolites and peraluminous rhyolites from the Glass House Mountains–Maleny–Noosa area, southeast Queensland, Australia. This rock association and the unique characteristics of the peralkaline rhyolites offer convincing lines of evidence that the petrogenesis of the peralkaline rhyolites is a straightforward consequence of protracted fractional crystallization from basaltic melts of alkali-rich composition. Compared to the common peraluminous rhyolites elsewhere, the peralkaline rhyolites here are characterized by elevated abundances of most incompatible elements, especially the very high Nb (vs. Th) and Ta (vs. U), the very low Ba, Sr and Eu and the extremely high $^{87}\text{Sr}/^{86}\text{Sr}$ ratio. The high Nb and Ta are inherited from the parental alkali basaltic melts. The low Ba, Sr and Eu result from removal of plagioclase during the protracted fractional crystallization. These rocks altogether define a Rb–Sr isochron of ~28 Ma, which is similar to Ar–Ar age data on these rocks in the literature. The extremely high $^{87}\text{Sr}/^{86}\text{Sr}$ ratio of the peralkaline rhyolites (up to 1.88) is actually characteristic of peralkaline rhyolites because of extreme Sr (also Eu and Ba) depletion and thus the very high Rb/Sr ratio. That is, the Sr in these rocks is essentially radiogenic ^{87}Sr accumulated from the ^{87}Rb decay since the volcanism. We suggest that the petrogenesis of the peralkaline rhyolites from the Glass House Mountain area may be of general significance globally.

The coeval peraluminous rhyolites apparently result from crustal anatexis in response to the basaltic magma underplating. The small “Daly Gap” exhibited in this rock association is anticipated during the protracted fractional crystallization from basaltic parent to the more evolved felsic varieties.

© 2014 Elsevier B.V. All rights reserved.

1. Introduction

Peralkaline volcanic rocks (with molar $[\text{Na}_2\text{O} + \text{K}_2\text{O}]/\text{Al}_2\text{O}_3 > 1$) are volumetrically minor but globally widespread (e.g., Bhushan et al., 2010; Heumann and Davies, 2002; Hong et al., 2013; Macdonald and Scaillet, 2006; Marshall et al., 2009; Ren et al., 2006; Renna et al., 2013; Rooney et al., 2012; Wei et al., 2007; White et al., 2006, 2009 and Zou et al., 2010). All the peralkaline rocks are of felsic composition (e.g., trachyte, rhyolites and phonolite); no mafic rocks are peralkaline because of the high Al_2O_3 and thus low $[\text{Na}_2\text{O} + \text{K}_2\text{O}]/\text{Al}_2\text{O}_3$. Macdonald (1974) divided peralkaline volcanic rocks into four groups (i.e., pantelleritic trachyte, comenditic trachyte, pantellerite, comendite) according to $\text{FeO}/(\text{FeO} + \text{MgO})$ and Al_2O_3 contents. Peralkaline volcanic rocks are commonly emplaced in continental rifts (e.g., Macdonald et al., 2012; Peccerillo et al., 2003; Ronga et al., 2010 and Scaillet and Macdonald,

2003) and on intra-plate ocean islands (e.g., Larsen, 1979; Bohrson and Reid, 1997 and Kar et al., 1998). Subduction-related peralkaline volcanic rocks have also been reported (e.g., Sardinia, Italy, Lustrino et al., 2004; Morra et al., 1994 and Parker et al., 2012).

The origin of peralkaline volcanic rocks remains a matter of debate. There are two major models: (1) low-volume end-products by protracted fractional crystallization of transitional to mildly alkali basalts (e.g., Mbassa et al., 2012; Peccerillo et al., 2003, 2007 and White et al., 2012) and (2) partial melting of old crust or mafic intrusive rocks (e.g., Black et al., 1997; Bohrson and Reid, 1997; Hong et al., 2013 and Macdonald et al., 1987). For example, Civetta et al. (1984, 1998) suggested that pantellerites from the type location Pantelleria island, Sicily channel, Italy, originated from fractional crystallization of alkali basalts. However, Lowenstein and Mahood (1991) consider that the pantellerites were produced by fractional crystallization of pantelleritic trachytes derived from partial melting of alkali gabbros.

In this paper, we illustrate the petrogenesis of the Oligocene (~28 Ma) peralkaline rhyolites from the Glass House Mountains–Maleny–Noosa area (GHM for short), southeastern Queensland,

* Corresponding authors at: Institute of Oceanology, Chinese Academy of Sciences, 7# Nanhai Road, Shiman District, Qingdao 266071, China. Tel.: +86 15652927971.

E-mail addresses: fenglishao@126.com (F. Shao), yaoling.niu@foxmail.com (Y. Niu).

Australia (Fig. 1) as the result of protracted fractional crystallization of alkali basaltic melts parental to the trachybasaltic lavas observed. We collected trachybasalts, syenites (containing mafic enclaves), trachytes, peralkaline rhyolites and peraluminous rhyolites from the GHM area. These coeval yet varying rock types represent the best sample suites with which to discuss the petrogenesis of peralkaline rhyolites. We present bulk-rock major and trace element data, and Sr, Nd and Pb isotopic compositions to demonstrate the validity and efficacy of our interpretation on the petrogenesis of the peralkaline rhyolites.

2. Geology

The Cenozoic intra-plate volcanism extends discontinuously along the eastern Australian continent for some 3000 km and is dominated by mafic lavas with varying amounts of volcanic and intrusive rocks of felsic composition, showing a compositional bimodality (Ewart, 1982; Ewart and Grenfell, 1985 and Ewart et al., 1988). The origin of this intra-plate magmatism has been widely discussed (see Johnson, 1989) and is best explained in terms of the mantle plume/hotspot hypothesis, especially because of the age progression recorded in a number of “central volcano complexes” that is consistent with northward drift of

the Australian plate (Cohen et al., 2007, 2013; Knesel et al., 2008; Sutherland et al., 2012; Wellman, 1989 and Wellman and McDougall, 1974) with the hotspot center probably located in the Bass Strait (Johnson, 1989). In this paper, we do not wish to discuss the mantle hotspot/plume magmatism and mantle dynamics, but use the unique and prime rock association from the GHM area to discuss one of the important petrological problems, i.e., the petrogenesis of peralkaline rhyolites. Fig. 1 shows the simplified geological map of the GHM area along the Sunshine Coast of southeastern Queensland, ~60 km north of Brisbane. The volcanic fields define a north-south belt of ~110 km.

The Glass House Mountains are a group of dome-shaped hills and plug peaks (Table 1) of peralkaline rhyolites and trachytes that rise abruptly from the coastal plain. These hypabyssal volcanic rocks intrude essentially horizontally bedded Late Triassic to Early Jurassic Landsborough sandstones (Cohen et al., 2007; Ewart and Grenfell, 1985). The Noosa felsic suite includes peralkaline rhyolites (isolated plugs), peraluminous rhyolites, syenites and granites (the only phaneritic intrusions in the study area). The peralkaline rhyolite plugs crosscut the Early to Middle Triassic Kin Kin Phyllite of the Gympie Block in the north part, and intrude the Triassic to Early Jurassic Myrtle Creek Sandstone in the south (Cohen et al., 2007).

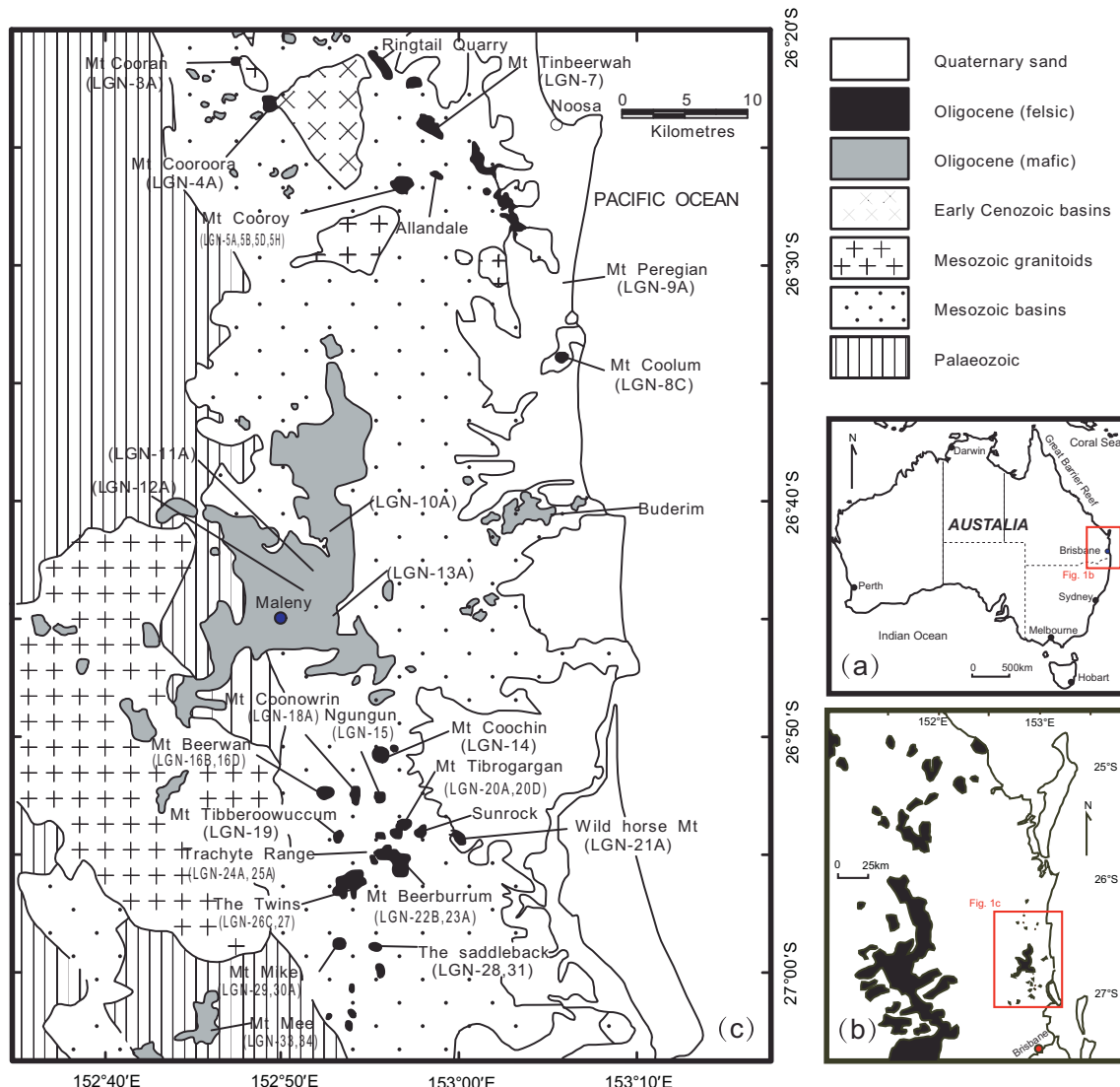


Fig. 1. (a) Simplified map of Australia. (b) Map of southeast Queensland with distribution of Cenozoic volcanic rocks. (c) Simplified geological map with sample localities and numbers (modified from Cohen et al., 2007).

Table 1

Information on samples, Glass House Mountains area, southeastern Queensland.

Sample	Location	GPS	Rock name ^a	Brief petrography	Data type
LGN-10	Mapleton	−26°41'55"S, 152°54'15"E	Basalt	Vesicular, porphyritic and altered, olivine altered to idingosite. ~5% phenocrysts of olivine (~1 mm, resorption texture), ~85% groundmass of plagioclase, olivine, clinopyroxene, orthopyroxene.	ME, TE, Sr, Nd, Pb
LGN-11A	Maleny	−26°43'20"S, 152°53'50"E	Trachybasalt	Massive and fresh; holocrystalline; intergranular texture; granular pyroxene and magnetite filled the clearance of enhedral plagioclase.	ME, TE
LGN-12A	Maleny	−26°44'45"S, 152°52'46"E	Trachybasalt	Massive and fresh; holocrystalline; intergranular texture; olivine (~15%), plagioclase (~40%), clinopyroxene (~40%), magnetite (~3%).	ME, TE, Sr, Nd, Pb
LGN-13A	Maleny	−26°47'06"S, 152°53'23"E	Trachybasalt	Porphyritic and fresh; ~15% phenocrysts of olivine, plagioclase, average grain size ~3 mm; ~85% groundmass of plagioclase (~45%), olivine (~15%), clinopyroxene (~15%), magnetite (<5%).	ME, TE
LGN-33	Mt Mee	−27°05'04"S, 152°38'23"E	Trachybasalt	Porphyritic and fresh; ~5% phenocrysts of plagioclase, average grain size ~3 mm; ~95% groundmass of plagioclase (~45%), olivine (~20%), clinopyroxene (~20%), magnetite (<5%), average grain size ~0.2 mm.	ME, TE
LGN-34	Mt Mee	−27°04'35"S, 152°38'54"E	Basaltic trachyandesite	Massive and fresh; cryptocrystalline texture; olivine (~25%), plagioclase (~50%), clinopyroxene (~15%), magnetite (<5%).	ME, TE, Sr, Pb
LGN-5A	Mt Cooroy	−26°25'49"S, 152°57'11"E	Syenite	Massive and fresh, porphyritic-like texture, ~30% "phenocrysts" of plagioclase, orthoclase, biotite, average grain size ~5 mm, ~70% "groundmass" of plagioclase, orthoclase, amphibole, biotite, quartz and magnetite.	ME, TE
LGN-5B	Mt Cooroy	−26°25'49"S, 152°57'11"E	Encalve in Syenite	Massive and fresh, amygdaloidal structure, ~30% "amygdaloid" of calcite (~5 mm, semi-directional), ~70% "groundmass" of plagioclase, orthoclase, amphibole, biotite, quartz and magnetite, average grain size 2 mm.	ME, TE
LGN-5D	Mt Cooroy	−26°25'49"S, 152°57'11"E	Encalve in Syenite	Massive and fresh, porphyritic-like texture, ~15% "phenocrysts" of plagioclase, orthoclase, biotite, average grain size ~5 mm, ~85% "groundmass" of plagioclase, orthoclase, amphibole, biotite, quartz and magnetite.	ME, TE, Sr, Nd, Pb
LGN-5H	Mt Cooroy	−26°25'49"S, 152°57'11"E	Encalve in Syenite	Massive and fresh, porphyritic-like texture, ~20% "phenocrysts" of plagioclase, orthoclase, biotite, average grain size ~5 mm, ~80% "groundmass" of plagioclase, orthoclase, amphibole, biotite, quartz and magnetite.	ME, TE
LGN-16B	Mt Beerwah	−25°32'53"S, 152°45'38"E	Comenditic trachyte	Massive and fresh, trachytic texture, microcrystals of alkali feldspar are approximately parallel. Feldspar streamline can bypass phenocrysts.	ME, TE, Sr, Nd
LGN-16D	Mt Beerwah	−25°32'37"S, 152°45'06"E	Comenditic trachyte	Massive and fresh, trachytic texture, <5% phenocrystal of orthoclase (~3 mm, enhedral or subhedral), groundmass contains plagioclase, orthoclase, amphibole, biotite and quartz, average grain size ~0.2 mm.	ME, TE
LGN-22B	Mt Beerburum	−26°55'50"S, 152°57'35"E	Trachyte	Massive and fresh, trachytic texture, ~5% phenocrystal of amphibole and biotite (~1 mm, xenomorphic), groundmass contains feldspar (~60%), quartz (~20%), amphibole and biotite (~10%), magnetite (<5%).	ME, TE
LGN-23A	Mt Beerburum	−26°55'52"S, 152°56'58"E	Trachyte	Massive and fresh, trachytic texture, ~5% phenocrystal of amphibole and biotite (~1 mm, xenomorphic), groundmass contains feldspar (~60%), quartz (~20%), amphibole and biotite (~10%), magnetite (<5%).	ME, TE, Sr, Nd, Pb
LGN-29	Mt Mike	−26°59'46"S, 152°53'37"E	Trachyte	Massive and fresh; porphyritic; ~35% phenocrystal of microcline (~5–8 mm), quartz and amphibole, subhedral or xenomorphic; ~65% groundmass of plagioclase, orthoclase, amphibole and quartz.	ME, TE
LGN-30A	Mt Mike	−26°59'39"S, 152°54'05"E	Comenditic trachyte	Massive and fresh, trachytic texture, <5% phenocrystal of orthoclase (~3 mm, enhedral or subhedral), groundmass contains plagioclase, orthoclase, amphibole, biotite and quartz, average grain size ~0.2 mm.	ME, TE
LGN-31	The Saddleback	−26°58'20"S, 152°54'53"E	Comenditic trachyte	Massive and fresh, trachytic texture, ~5% phenocrystal of amphibole and biotite (~1 mm, xenomorphic), groundmass contains feldspar (~60%), quartz (~20%), amphibole and biotite (~10%), magnetite (<5%).	ME, TE, Sr, Pb
LGN-3A	Mt Cooran	−26°20'12"S, 152°40'40"E	Comendite	Massive and fresh; porphyritic; ~25% phenocrystal of plagioclase and orthoclase (~20%, interpenetration twin) and quartz (~5%); average grain size ~1 mm; ~75% groundmass of plagioclase, orthoclase, quartz and amphibole.	ME, TE, Sr, Nd, Pb
LGN-4A	Mt Cooroora	−26°22'13"S, 152°50'37"E	Comendite	Massive and fresh; fluidal structure; porphyritic; ~30% phenocrystal of plagioclase and orthoclase (~25%) and quartz (~5%); average grain size ~1 mm; ~75% groundmass of plagioclase, orthoclase, quartz and amphibole.	ME, TE
LGN-8C	Mt Coolum	−26°33'51"S, 153°05'18"E	Comendite	Massive; fluidal structure; cryptocrystalline; amphibole slightly altered.	ME, TE, Sr, Nd, Pb
LGN-14	Mt Coochin	−26°52'25"S, 152°55'52"E	Comendite	Massive and fresh; fluidal structure; porphyritic; ~15% phenocrystal of quartz and orthoclase (~10%) and quartz (~5%); average grain size ~3 mm; ~85% groundmass of plagioclase, orthoclase, quartz and amphibole.	ME, TE
LGN-15	Mt Ngungun	−26°53'59"S, 152°54'40"E	Comendite	Massive and fresh; fluidal structure; porphyritic; ~5% phenocrystal of quartz and orthoclase, average grain size ~3 mm; ~85% groundmass of plagioclase, orthoclase, quartz and amphibole, average grain size 0.5 mm.	ME, TE, Sr, Pb
LGN-18A	Mt Coonowrin	−26°54'01"S, 152°54'40"E	Comendite	Massive and fresh; porphyritic; ~25% phenocrystal of quartz and orthoclase, average grain size ~2 mm; ~75% groundmass of plagioclase, orthoclase, quartz and amphibole, average grain size 0.2 mm.	ME, TE, Sr, Pb
LGN-19A	Mt Tibberoowuccum	−26°56'01"S, 152°55'41"E	Comendite	Massive and fresh; porphyritic; ~30% phenocrystal of quartz, orthoclase and amphibole, average grain size ~2 mm; ~70% groundmass of plagioclase, orthoclase, quartz and amphibole, minor magnetite, average grain size 0.2 mm.	ME, TE, Sr, Nd, Pb

Table 1 (continued)

Sample	Location	GPS	Rock name ^a	Brief petrography	Data type
LGN-20A	Mt Tibrogargan	–26°55'41"S, 152°56'29"E	Comendite	Massive and fresh; porphyritic; ~5% phenocrystal of quartz and orthoclase (~2 mm); ~95% groundmass of plagioclase, orthoclase, quartz and amphibole, minor magnetite, augite, aegirine and arfvedsonite (~5%), average grain size 0.1 mm.	ME, TE
LGN-20D	Mt Tibrogargan	–26°55'41"S, 152°56'29"E	Comendite	Massive and fresh; porphyritic; ~5% phenocrystal of quartz and orthoclase, average grain size ~2 mm; ~95% groundmass of plagioclase, orthoclase, quartz and amphibole, minor magnetite, augite, aegirine and arfvedsonite (~5%), average grain size 0.1 mm.	ME, TE, Pb
LGN-21A	Wild Horse Mt		Comendite	Massive and fresh, fluidal structure; cryptocrystalline, quartz (~25%), orthoclase (~35%), plagioclase (~25%), amphibole (~10%), augite, aegirine and arfvedsonite (~5%).	ME, TE, Sr, Pb
LGN-24A	Trachyte Range	–26°57'10"S, 152°57'02"E	Comendite	Massive and slightly altered, amphibole altered to chlorite/epidote, biotite-bearing.	ME, TE
LGN-25A	Trachyte Range	–26°54'05"S, 152°56'14"E	Comendite	Massive and fresh, fluidal structure; cryptocrystalline. No thin section.	ME, TE, Sr, Nd, Pb
LGN-26C	The Twins-big	–26°57'44"S, 152°53'44"E	Comendite	Massive and fresh; porphyritic; ~5% phenocrystal of quartz and orthoclase, hypidiomorphic, average grain size ~4 mm; ~95% groundmass of plagioclase, orthoclase, quartz and amphibole, minor magnetite, augite, aegirine and arfvedsonite (~5%), average grain size 0.2 mm.	ME, TE, Sr, Nd, Pb
LGN-27	The Twins-small	–26°58'02"S, 152°53'41"E	Comendite	Massive and fresh; porphyritic; ~5% phenocrystal of quartz and orthoclase, anhedral, average grain size ~4 mm; ~95% groundmass of plagioclase, orthoclase, quartz and amphibole, minor magnetite, augite, aegirine and arfvedsonite (~5%), average grain size 0.2 mm.	ME, TE
LGN-28	The Saddleback	–26°58'56"S, 152°53'49"E	Comendite	Massive and fresh; porphyritic; ~5% phenocrystal of quartz and orthoclase, anhedral, average grain size ~4 mm; ~95% groundmass of plagioclase, orthoclase, quartz and amphibole, minor magnetite, augite, aegirine and arfvedsonite (~5%), average grain size 0.2 mm.	ME, TE
LGN-7	Mt Tinbeerwah	–26°23'01"S, 152°58'03"E	Peraluminous rhyolite	Massive and fresh, cryptocrystalline. Biotite-bearing (~5%), quartz (~25%), feldspar (~60%).	ME, TE, Sr, Nd, Pb
LGN-9A	Mt Peregian	–26°30'18"S, 152°59'41"E	Peraluminous rhyolite	Massive and fresh, vesicular structure, porphyritic, ~5% phenocrystal of quartz and biotite, subhedral-anhedral, average grain size ~3 mm, ~95% groundmass of quartz (~25%), feldspar (~60%) and biotite (~5%).	ME, TE

^a The rock names were classified by total alkalis vs. silica classification diagram. ME, major elements; TE, trace elements; Sr, Nd, and Pb, isotopes.

Basaltic lavas around the town of Maleny cover an area of ~200 km² (Fig. 1). These lavas are compositionally termed here as trachybasalts (Fig. 2a). They overlie unconformably the Mesozoic Nambour Basin and the older metamorphic rocks of the D'Aguilar Block (Cohen et al., 2007 and Ewart and Grenfell, 1985). Most of the Glass House Mountain peaks rise above the top level defined by the top of the Maleny lavas, which allowed Stevens (1989) to infer that the upper parts of some prominent peaks were probably extrusive. This may be true if the Maleny basalt sequence was not much higher since eruption at ~28 Ma. However, no felsic lavas or pyroclastic rocks have been recognized. We infer that both sub-aerial felsic lavas and pyroclastic rocks must have been eroded away. The trachybasalts also crop out in the Mt Mee area, southwest of the Glass House Mountains.

3. Samples and petrography

We sampled all the igneous rock types in the GHM area (see Fig. 1, Table 1), including trachybasalts of Maleny and Mt. Mee, peralkaline rhyolites and trachytes of Glass House Mountains, peralkaline rhyolites, syenite and peraluminous rhyolites of Noosa. The trachybasalts are dominantly porphyritic or holocrystalline, containing phenocrysts of olivine and plagioclase (average grain size ~3 mm). The Mt. Cooroy syenite is the only phaneritic intrusion sampled in the study area. Note that enclaves of mafic to intermediate composition have been found in the syenite intrusion. The enclaves have porphyritic-like texture. Trachytes have characteristic trachytic texture. Both hand specimen and thin-section of the peralkaline rhyolites (comendites) show light blue owing to the alkaline minerals such as albite aegirine, arfvedsonite, and riebeckite. The peraluminous rhyolites are cryptocrystalline or porphyritic, with minor phenocryst of quartz, biotite, sanidine and plagioclase. Table 1 summarizes the sample details, including sample locations, rock types, concise petrography, and types of analytical work done.

4. Analytical methods

All the samples are fresh with all the surfaces removed using a diamond mill. The samples were then crushed using a percussion mill into 1–2 cm fragments, which were then ultrasonically cleaned in Milli-Q water, dried, and powdered in a thoroughly cleaned agate mill in the clean laboratory at the University of Queensland (UQ). Sample powders in ultraclean Teflon beakers were placed in a clean oven at 110 °C overnight before being weighed and acid digested.

Bulk-rock major elements (Appendix Table 1) were analyzed using a Perkin Elmer Optima 3300 DV inductively coupled plasma-optical emission spectroscopy (ICP-OES) system at UQ following the procedure of Fang and Niu (2003) and Kwiecien (1990). Precision (1σ) for most elements based on U.S. Geological Survey (USGS) standards (AGV-1, BCR-1, and BIR-1) is <1% with the exception of TiO₂ (1.3%) and P₂O₅ (2.0%). Bulk-rock trace element abundances (Appendix Table 1) were analyzed on a Fisons Plasma QuadII ICP-MS system at UQ with analytical conditions and procedures following Niu and Batiza (1997). Trace element data for the USGS standard reference materials AGV-1 and BIR-1 and blank levels analyzed are given in Appendix Table 2.

For Sr and Nd isotope analyses, 100–150 mg of rock powder was dissolved in HF–HNO₃ mix and brought into solution in HCl. Sr and the rare earth elements (REEs) were separated through cation ion exchange columns, Nd was then separated from the other REEs using a conventional bis (2-ethylhexyl) hydrogen phosphate (HDEHP) method. Pb isotope analyses were carried out on a separate dissolution using the technique following Regelous et al. (1999). Blanks were below 0.7, 0.4, and 0.2 ng for Sr, Nd and Pb, respectively. All the isotope measurements were carried out at UQ on a Fisons VG Sector 54-30 thermal ionization mass spectrometer in static mode. For Sr and Nd isotopic analyses, an exponential fractionation correction was applied using ⁸⁶Sr/⁸⁸Sr = 0.1194 and ¹⁴⁶Nd/¹⁴⁴Nd = 0.7219. Mean values for the NBS987 Sr standard over the period of analysis yielded ⁸⁷Sr/⁸⁶Sr = 0.710267 ± 15 (2σ),

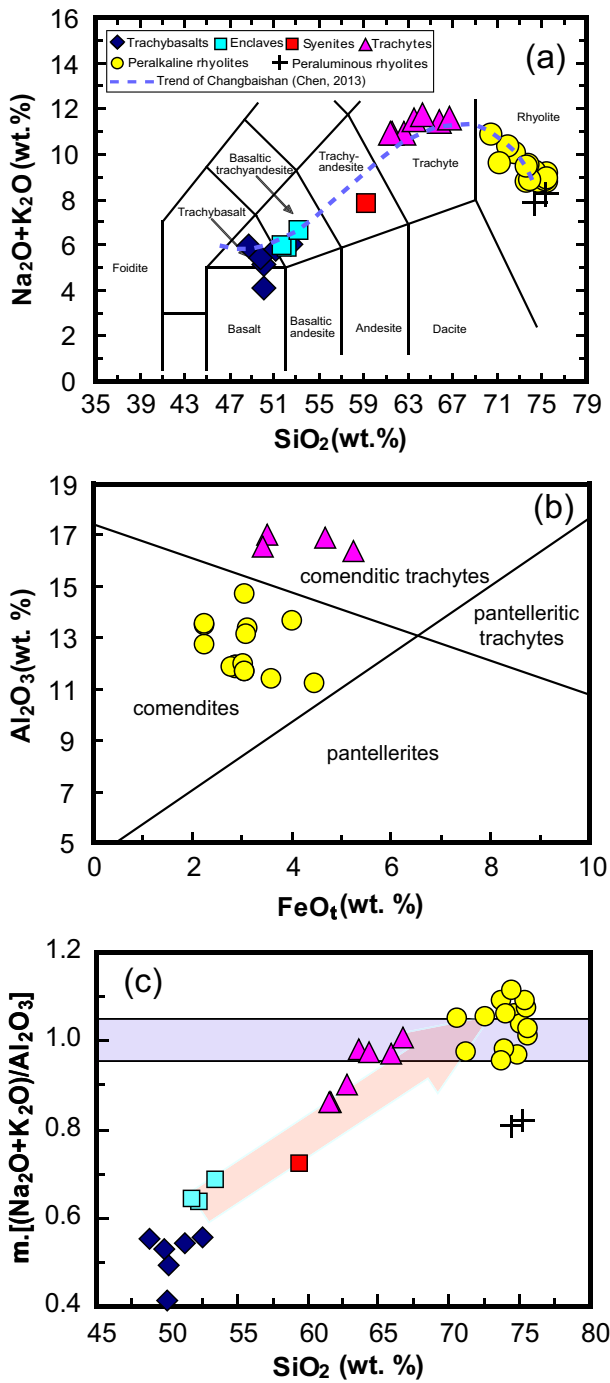


Fig. 2. (a) Total alkalis vs. silica diagram (Le Bas et al., 1986) to show the bimodal volcanic rocks from the Maleny–Glass House Mountains–Noosa area (or GHM area for short), southeast Queensland. One syenite sample and enclaves are also plotted for comparison. The dashed line represents the liquid line of descent defined by the Quaternary volcanic rocks from Changbaishan (Northeast China) from alkali basalts to comendites (Chen, 2013). (b) Al_2O_3 vs. FeO_{t} diagram (Macdonald, 1974) to further classify peralkaline rocks. (c) Peralkalinity index, i.e., $PI = \text{molar } [\text{Na}_2\text{O} + \text{K}_2\text{O}]/\text{Al}_2\text{O}_3$ shows linear increasing trend with increasing SiO_2 . Considering the analytical error (the light-blue band), the evolved trachytes and all the rhyolites are peralkaline except for the two peraluminous rhyolite samples. (For interpretation of the references to color in this figure legend, the reader is referred to the web version of this article.)

and the Ames Nd standard gave $^{143}\text{Nd}/^{144}\text{Nd} = 0.511969 \pm 9$ (2σ). Pb isotope measurements were corrected for mass fractionation (typically 1.4% per amu) determined from 2 to 3 analyses of the NBS 981 Pb standard during each run. Some samples were digested and analyzed

several times with the reported values reproducible within analytical error.

5. Results

5.1. Major elements

The total alkalis vs. silica (TAS) diagram (Fig. 2a) shows that our samples define a compositional spectrum from mafic to felsic. With the exception of more evolved LGN-34 which can be classified as basaltic trachyandesite and LGN-10 that has the lowest total alkalis (4.16 wt.%) and highest LOI values (4.52 wt.%), the mafic rocks are dominantly trachybasalts. Considering that the syenite and its mafic enclaves may represent the compositional transition from basalts to the more felsic rocks, they are also plotted for comparison. Given the analytical uncertainties, samples with the peralkalinity index PI (molar $[\text{Na}_2\text{O} + \text{K}_2\text{O}]/\text{Al}_2\text{O}_3 \geq 0.95$) are considered peralkaline. With this criterion, 4 evolved trachyte samples and all (but two peraluminous samples) rhyolite samples can be classified, respectively, as comenditic trachyte and comendite two peralkaline sub-types in Al_2O_3 - FeO space (Fig. 2b). The significant linear trend between the PI and SiO_2 defined by all the samples (but two peraluminous rhyolites; Fig. 2c) manifests their genetic link readily explained by Ca-rich plagioclase crystallization (see below).

On SiO_2 -variation diagrams (Fig. 3), these rocks define, to a first-order, liquid lines of descent, evolving from trachybasalts through trachytes to peralkaline rhyolites with increasing SiO_2 . The light blue dashed curves are best-fit regression lines representing the liquid lines of descent defined by the Quaternary alkali basalt–peralkaline rhyolite suite of Changbaishan in Northeast China (Chen, 2013). The mafic enclaves resemble trachybasalts with, on average, higher SiO_2 and lower MgO .

If we exclude the intrusive syenite and enclaves, the bulk of the volcanic rocks altogether show a bimodality, with an apparent “Daly Gap” (i.e., the paucity of intermediate rocks, ~53–62 wt.% SiO_2 ; Daly, 1925; Figs. 3, 4), as most of the eastern Australia bimodal suites (Ewart, 1982; Ewart and Grenfell, 1985 and Ewart et al., 1988). Ewart and Grenfell (1985) reported a younger summit lava in the Maleny sequence whose composition (54 wt.%) overlaps the Daly Gap. Meanwhile, the adjacent Bunya Mountains sequence and Main Range sequence also include several flows of trachyandesites and benmoreite with SiO_2 within the Daly Gap. As we suggested above that higher level evolved lavas may have been removed by erosion, such removal could well include further lavas within the Daly interval. So, the Gap between the Maleny mafic flow sequence and the Glass House silicic intrusives perhaps less marked than apparent in our sample set.

5.2. Trace elements

Trace element compositions of the GHM rocks are also consistent, to a first order, with liquid lines of descent (see Fig. S1). Compatible trace elements, such as Co and Cr (not shown, but also true for V, Ni and Sc) decrease with increasing SiO_2 , whereas incompatible trace elements such as Nb and Hf increase with increasing SiO_2 as expected (Fig. S1). The variations of $[\text{La}/\text{Sm}]_N$ and $[\text{Sm}/\text{Yb}]_N$ with increasing SiO_2 (Fig. S1) are also consistent with liquid lines of descent. However, the “anomalously” varied and lowered values at the high SiO_2 rhyolite end reflect crystallization of alkali feldspars (e.g., anorthoclase) from such peralkaline melts with $D_{\text{La}} > D_{\text{Sm}} > D_{\text{Yb}}$ (Mahood and Stimac, 1990). See caption to Fig. S1 for details.

As a whole, the samples are light REE (LREE) enriched (e.g., $[\text{La}/\text{Sm}]_N > 1$, $[\text{Sm}/\text{Yb}]_N > 1$; Figs. 4, S2), with $[\text{La}/\text{Yb}]_N$ up to 15.8. The REE patterns of trachybasalts are similar to average composition of ocean island basalts (OIB; Sun and McDonough, 1989) with a weak positive Eu anomaly (i.e., $\text{Eu}/\text{Eu}^* \geq 1.0$). Trachytes and peralkaline rhyolites both show varying large negative Eu anomalies reflecting significant

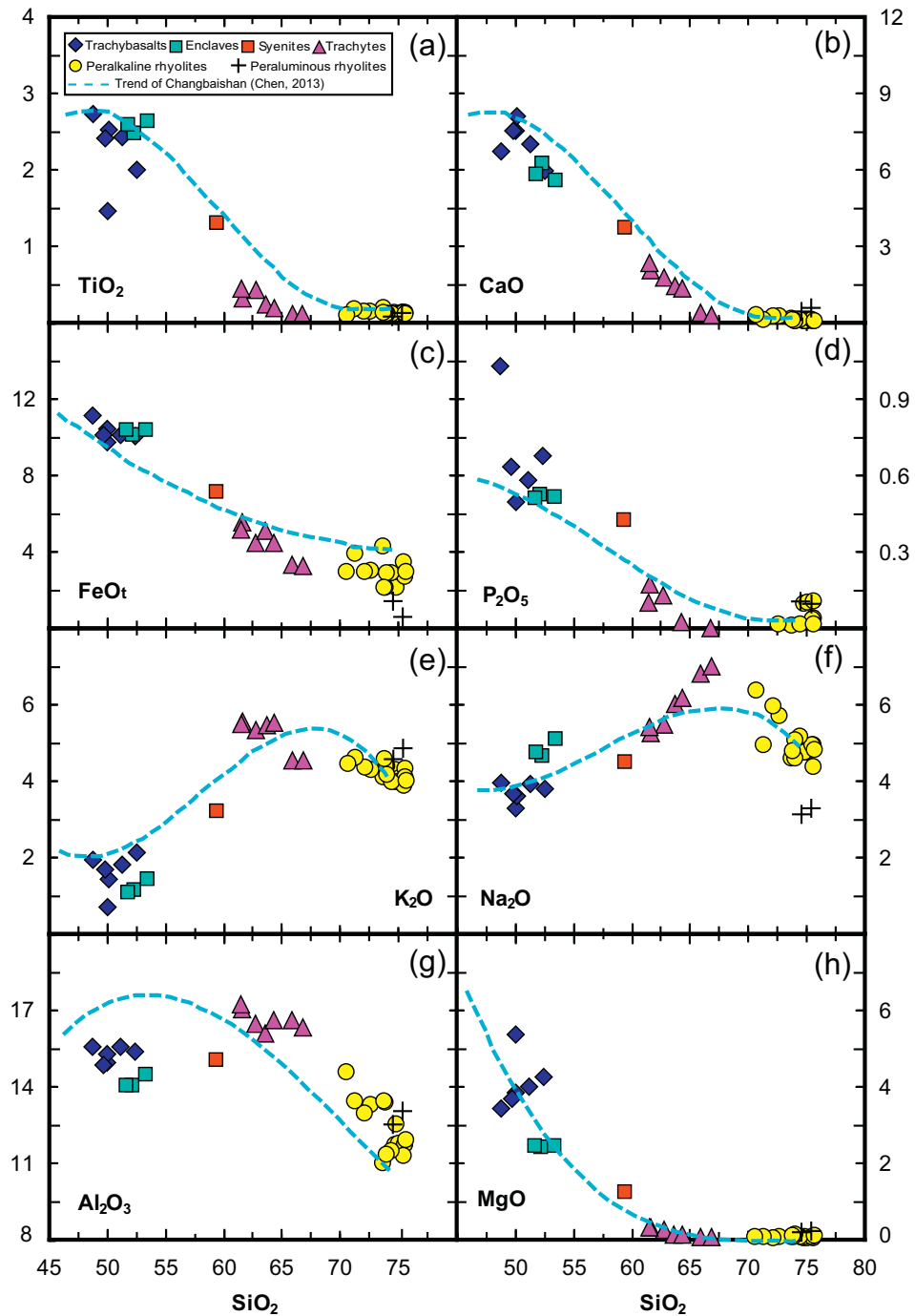


Fig. 3. SiO_2 variation diagrams for major elements (wt.%). TiO_2 , CaO , FeO_{t} , P_2O_5 and MgO decrease with increasing SiO_2 , K_2O , Na_2O and Al_2O_3 increase and then decrease at different SiO_2 values with increasing SiO_2 , which explains the monotonic increase of PI with increasing SiO_2 (see Fig. 2c). The syenite and its contained enclaves plot along the curved trends between trachybasalts and trachytes. The dashed curve is the liquid line of descent defined by the Quaternary Changbaishan volcanic rocks of Northeast China (Chen, 2013; see Fig. 2a). Also see SiO_2 variation diagrams for trace element data in Fig. S1. (For interpretation of the references to color in this figure legend, the reader is referred to the web version of this article.)

plagioclase crystallization (see Niu & O'Hara, 2009). Both negative and positive Ce anomalies are observed in trachytes and peralkaline rhyolites ($\text{Ce}/\text{Ce}^* = 0.49\text{--}3.69$; $\text{Ce}/\text{Ce}^* = 2^*\text{Ce}_{\text{N}}/[\text{La}_{\text{N}} + \text{Pr}_{\text{N}}]$), suggesting the presence of a significant fraction of the element Ce as Ce^{4+} (vs. the common Ce^{3+}) that behaves differently from Ce^{3+} and its neighboring La^{3+} and Pr^{3+} . For example, LGN-16B and LGN-16D are from the same locality in Mt. Beerwah, and show both negative and positive Ce anomalies (Figs. 4, S2). The Ce anomalies most likely result from crystallization and resorption of mineral phases with abundant +4 cations such as zircon, which is likely to have abundant Ce^{4+} in replacement of Zr^{4+} as shown in all zircon REE analyses in the abundant

literature. In this context, it is worth to point out that Ce^{4+} (together with Ce^{3+}) always exists in nature, but its presence is better expressed in minerals, rocks and melts directly related to or highly effected by minerals with abundant +4 cations like zircons. Similarly, Eu^{2+} (along with Eu^{3+}) also always exists in nature (Niu and O'Hara, 2009), but its presence is better manifested in minerals, rocks and melts directly related to or highly affected by plagioclase, in which Eu^{2+} (vs. all other 3^+ REEs) is compatible. Hence, $\text{Ce}^{4+}/\text{Ce}^{3+}$ ratio (and also $\text{Eu}^{2+}/\text{Eu}^{3+}$) is not a reliable indicator for redox conditions (Niu and O'Hara, 2009), but inherited from parental melts or even magma sources.

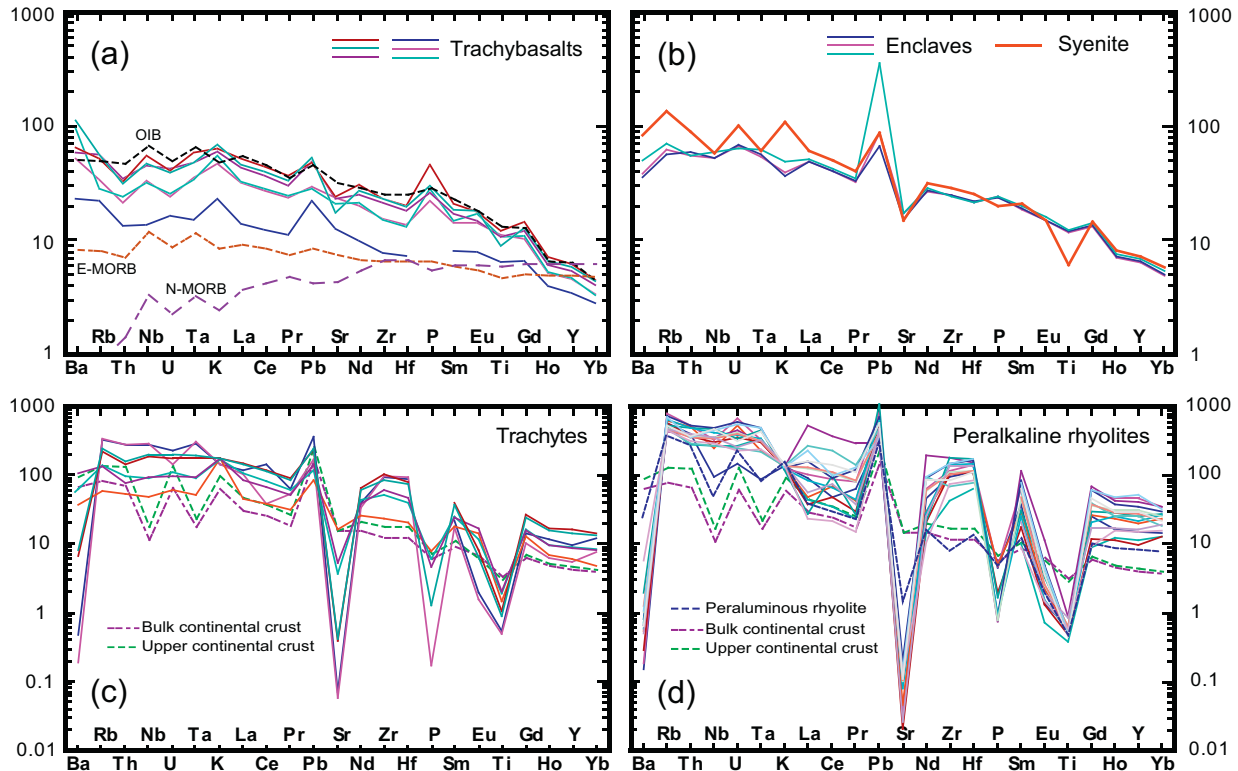


Fig. 4. Primitive mantle (Sun and McDonough, 1989) normalized multi-element diagrams to show that trachytes and peralkaline rhyolites have variably higher abundances of most incompatible elements than peraluminous rhyolites and continental crust compositions with characteristic features: (i) high, NOT low, Nb (vs. Th) and Ta (vs. U) inherited from alkali basalts parental to trachybasalts; (ii) excess depletion of Ba, Sr, and Eu as a result of plagioclase and K-feldspar separation during the protracted fractional crystallization; and (iii) excess P and Ti depletion of apatite and titanomagnetite separation at the trachyte stage during the fractional crystallization. Average OIB, E-MORB, N-MORB, bulk continental crust and upper continental crust are plotted for comparison (Rudnick and Gao, 2003; Sun and McDonough, 1989). Also see Figs. S2 and S3.

Peralkaline rhyolites have extremely low abundances of Ba, Sr, Eu, P and Ti (e.g., $\text{Sr/Sr}^* < 0.01$; $\text{Eu/Eu}^* = 0.15\text{--}0.01$; Figs. 4, S3) and high Nb and Ta contents with Nb^* and Ta^* significantly greater than those of peraluminous rhyolites, continental crustal materials and island arc basalts (Fig. 5). The peralkaline rhyolites have variably high Nb/Ta (15.97–21.71), similar to or even higher than average mid-ocean ridge basalts (MORB) and ocean island basalts (OIB), and distinctively higher than peraluminous rhyolites and continental crustal materials (Fig. 5).

All these features indicate that the petrogenesis of peralkaline rhyolites differs from the common peraluminous rhyolites (see below).

5.3. Sr, Nd and Pb isotope data

The $^{87}\text{Sr}/^{86}\text{Sr}$ ratios of trachybasalts and enclaves from syenite are restricted to 0.70419–0.70431, but most trachytes and peralkaline rhyolites have unexpectedly high ratios, ranging from 0.70564 to 1.87669 (Appendix Table 3; Fig. 6). Samples with very high $^{87}\text{Sr}/^{86}\text{Sr}$ ratios all have extremely low Sr content (<10 ppm) and high Rb/Sr ratios (>100, Fig. S4a). This is a straightforward consequence of Sr (also low Ba and Eu) depletion as the result of plagioclase (and to some extent alkali feldspars) removal during the protracted fractional crystallization. That is, the Sr in the peralkaline rocks is essentially all radiogenic ^{87}Sr accumulated from ^{87}Rb decay since the volcanism.

Nd isotope data (Appendix Table 3) for all the rock types from the GHM area are essentially the same within a restricted $^{143}\text{Nd}/^{144}\text{Nd}$ range (0.512549–0.512655) or $\varepsilon_{\text{Nd}}(t) = -0.07$ to -1.44 (Fig. S4b), suggesting that they are cogenetic and share similar parental magmas. The correlated three Pb isotope ratio variations (Appendix Table 3) are interesting, especially the first-order increase of $[^{206}\text{Pb}/^{204}\text{Pb}]_{\text{initial}}$ (corrected to 28 Ma), $[^{207}\text{Pb}/^{204}\text{Pb}]_{\text{initial}}$ and $[^{208}\text{Pb}/^{204}\text{Pb}]_{\text{initial}}$ from trachybasalts to trachytes and to the peralkaline rhyolites (Fig. S4c–d; Appendix Table 3). This could be interpreted as resulting from

progressive crustal contamination of mantle melts parental to the trachybasalts. However, the uniform Nd isotope composition and essentially the same initial $^{87}\text{Sr}/^{86}\text{Sr}$ (Fig. 6b, d) as well as the high Nb and Ta for all these samples (except the two peraluminous rhyolites; Fig. 5a) indicate that crustal contamination, if any, is volumetrically rather insignificant. Nevertheless, the lack of Pb isotope correlations with U/Pb, Th/Pb, Pb and other compositional variables suggest that contamination with Pb isotopically heterogeneous crustal lithologies remains possible, but the ineffective homogenization explains the small scale and large magnitude Pb isotopic heterogeneity in our samples (Bryce and DePaolo, 2004; see Fig. S5 caption for details).

6. Discussion

The data and foregoing discussion suggest that the petrogenesis of the GHM peralkaline rhyolites is most consistent with their derivation through extensive fractional crystallization of alkaline basalts parental to the trachybasalts. We elaborate below the evidence in support of this interpretation.

6.1. The coevality

The close association of these varying rock types (Fig. 2) in time and space offers convincing evidence that these rocks are cogenetic. They cover an area of ~80 km from north to south with a width of ~30 km (Fig. 1), and share a $^{40}\text{Ar}/^{39}\text{Ar}$ age progression from 28.9 Ma on Maleny trachybasalts to 27.8 Ma on Mt. Cooroy monzonite, to 26.9 Ma on Glass House Mountains peralkaline rhyolites (see Cohen et al., 2007). This temporal and spatial consistency indicates that these rocks must be products of the same thermal/magmatic events and thus provide an unprecedented opportunity to study the petrogenesis of peralkaline rhyolites in a geodynamically active geological context. That is, the alkali

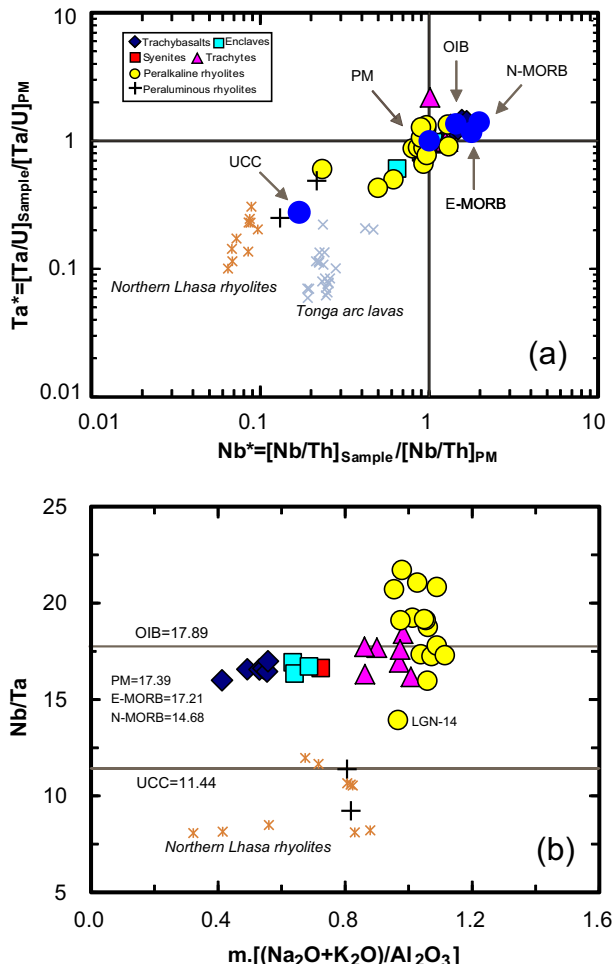


Fig. 5. (a) Nb^*-Ta^* anomaly diagram (after Niu et al., 1999). $\text{Nb}^* = [\text{Nb}/\text{Th}]_{\text{sample}}/[\text{Nb}/\text{Th}]_{\text{PM}}$, $\text{Ta}^* = [\text{Ta}/\text{U}]_{\text{sample}}/[\text{Ta}/\text{U}]_{\text{PM}}$ (after Niu and Batiza, 1997; Niu et al., 1999). The distinctive high Nb^* and Ta^* of peralkaline rhyolites demonstrate their inheritance from mantle derived basaltic melts with high Nb and Ta; crustal rocks have too low Nb and Ta plotted in the lower left quadrant (Niu and O'Hara, 2009). (b) Nb/Ta of the GHM volcanic rocks is high and comparable with mantle derived basalts (e.g., OIB, E-MORB, N-MORB) except for the two peraluminous rhyolites whose Nb/Ta ratios are characteristically low, similar to those of peraluminous rhyolites and continental crust. Average OIB, E-MORB, N-MORB (Niu and O'Hara, 2003), primitive mantle (PM; Sun and McDonough, 1989), upper continental crust (UCC; Rudnick and Gao, 2003), and peraluminous rhyolites from Northern Lhasa terrane (Chen et al., 2014; Sui et al. 2013) and Tonga arc lava (Ewart et al., 1998) data are plotted for comparison.

basaltic melts parental to the GHM trachybasalts impart the high alkali contents and high Nb (vs. Th) and Ta (vs. U) characteristic of peralkaline rhyolites. Protracted fractional crystallization of alkaline basaltic melts by plagioclase and K-feldspar gives rise to the properties of peralkaline rhyolites such as the extreme depletion of Ba, Eu and Sr and elevated Rb/Sr ratio.

6.2. Inherited high Nb-Ta

Compared with the peraluminous rhyolites (e.g., Samples LGN-7 and LGN-9A), peralkaline rhyolites from the GHM area and elsewhere characteristically have high Nb and Ta (Figs. 4, S3b). This is best shown in Nb^*-Ta^* space (Fig. 5a; Niu et al., 1999). Niu and Batiza (1997) show that during mantle melting and much of the basaltic magma evolution (e.g., olivine-clinopyroxene-plagioclase crystallization) $D_{\text{Nb}} \approx D_{\text{Th}} < D_{\text{Ta}} \approx D_{\text{U}}$, suggesting that Nb/Th and Ta/U ratios in magmatic processes do not change. It follows that the varying Nb/Th (or Nb^*) and Ta/U (or Ta^*) in magmatic rocks must have been inherited from their sources or source histories. Fig. 5a shows that in contrast to

the peraluminous rhyolites with $\text{Nb}^* < 1$ and $\text{Ta}^* < 1$ (samples LGN-7 and LGN-9A and the literature data), all of our GHM samples, including the peralkaline rhyolites, show $\text{Nb}^* \geq 1$ and $\text{Ta}^* \geq 1$ (except for 3 samples; see below). This is a magma source signature and the GHM peralkaline rhyolites inherit the high Nb^* and Ta^* from the alkali basaltic melts parental to the GHM trachybasalts. Because peralkaline rhyolites are highly evolved and must have experienced Ti-Fe oxide (titanomagnetite or pseudobrookite) fractionation earlier at the trachyte stage of 55–60% SiO_2 , which depletes both Ti and Fe in the melt (see Figs. 3a, c, 4c-d, 7g-h) as well as Nb (vs. Th) and Ta (vs. U) to some extent because of $Kd_{\text{Nb}} > Kd_{\text{Th}}$ and $Kd_{\text{Ta}} > Kd_{\text{U}}$ for Ti-Fe oxides (Niu and O'Hara, 2009), the peralkaline rhyolites should have slightly lower Nb^* and Ta^* than the trachybasalts, including the more depleted three samples (Fig. 5a). Three comendites (LGN-3A, LGN-4A and LGN-8C) sampled from Noosa area have small negative Nb^* and Ta^* because they have undergone more (than others) titanomagnetite (taking Nb and Ta) separation with depleted Fe and Ti (see Figs. 3 and 4).

To emphasize the concept of source inheritance and for comparison, we plot in Fig. 5a also mid-ocean ridge basalts (MORB) and ocean island basalts (OIB) with $\text{Nb}^* \geq 1$ and $\text{Ta}^* \geq 1$, upper continental crust and peraluminous rhyolites in the literature with $\text{Nb}^* < 1$ and $\text{Ta}^* < 1$.

Fig. 5b further demonstrates that in contrast to the low Nb/Ta (<~12) of continental crust and peraluminous rhyolites, the GHM trachybasalts, trachytes and peralkaline rhyolites all have elevated Nb/Ta ratios as high as or higher than that of MORB and OIB, manifesting the inherited high Nb/Ta from OIB-like alkali basalts. The apparently higher Nb/Ta of trachytes and peralkaline rhyolites than trachybasalts is consistent with the observation that Nb is slightly more incompatible than Ta during magma evolution (Niu and Batiza, 1997 and Niu and Hékinian, 1997).

6.3. Effect of plagioclase (also alkali feldspar) during protracted fractional crystallization

On SiO_2 -variation diagrams all the rock types define trends that are most consistent with liquid lines of descent (Figs. 2a, c, 3, S1) with peralkaline rhyolites being the final products. The early stage evolution of alkali basalts is dominated by fractional crystallization of olivine and clinopyroxene followed by the participation of plagioclase crystallization. The most primitive trachybasalts from the GHM area are quite evolved with $\text{MgO} \leq 5.0$ wt.%. Olivine, clinopyroxene and plagioclase will continue to crystallize as the melt continues to cool (decreasing MgO), but plagioclase is the key liquidus phase that dictates the melt composition towards peralkaline characteristics, i.e., extreme depletion of Sr, Eu, and Ba and thus elevated Rb/Sr. Note that crystallization of K-feldspar at the trachytic stage and thereafter will strengthen these peralkaline characteristics because K-feldspar acts the same as plagioclase with $Kd_{\text{Sr}} \gg 1$, $Kd_{\text{Eu}} \gg 1$, $Kd_{\text{Ba}} \gg 1$ and $Kd_{\text{Rb}} < 1$ (from GERM data base: <http://earthref.org/KDD/>).

6.3.1. Effect of plagioclase crystallization on major elements

The peralkalinity index PI is defined as molar $[\text{Na}_2\text{O} + \text{K}_2\text{O}]/\text{Al}_2\text{O}_3$ or $[\text{Na} + \text{K}]/\text{Al}$. Hence, crystallization of plagioclase, especially Ca-rich plagioclase during earlier stage of basaltic magma evolution, exerts the primary major element control towards peralkaline melt composition. This is because crystallization of Ca-rich plagioclase ($\text{Ca}[\text{Al}_2\text{Si}_2\text{O}_8]$) with $\text{Al}/\text{Ca} = 2$ depletes Al and enriches $[\text{Na} + \text{K}]$, hence increasing the PI , i.e., $[\text{Na} + \text{K}]/\text{Al}$, in the residual evolving melt. This is well manifested in Fig. 2c, where $[\text{Na} + \text{K}]/\text{Al}$ increases with increasing SiO_2 in the course of melt evolution from trachybasalts through trachytes to the peralkaline rhyolites.

6.3.2. Effect of plagioclase crystallization on Eu/Eu^* and Sr/Sr^*

Eu/Eu^* and Sr/Sr^* decrease sharply with increasing SiO_2 (49–62 wt.%; Fig. S5a, c) and show significant correlation between the two ($R^2 = 0.878$; Fig. 6a). This is a straightforward consequence of plagioclase-dominated fractionation because plagioclase is the only

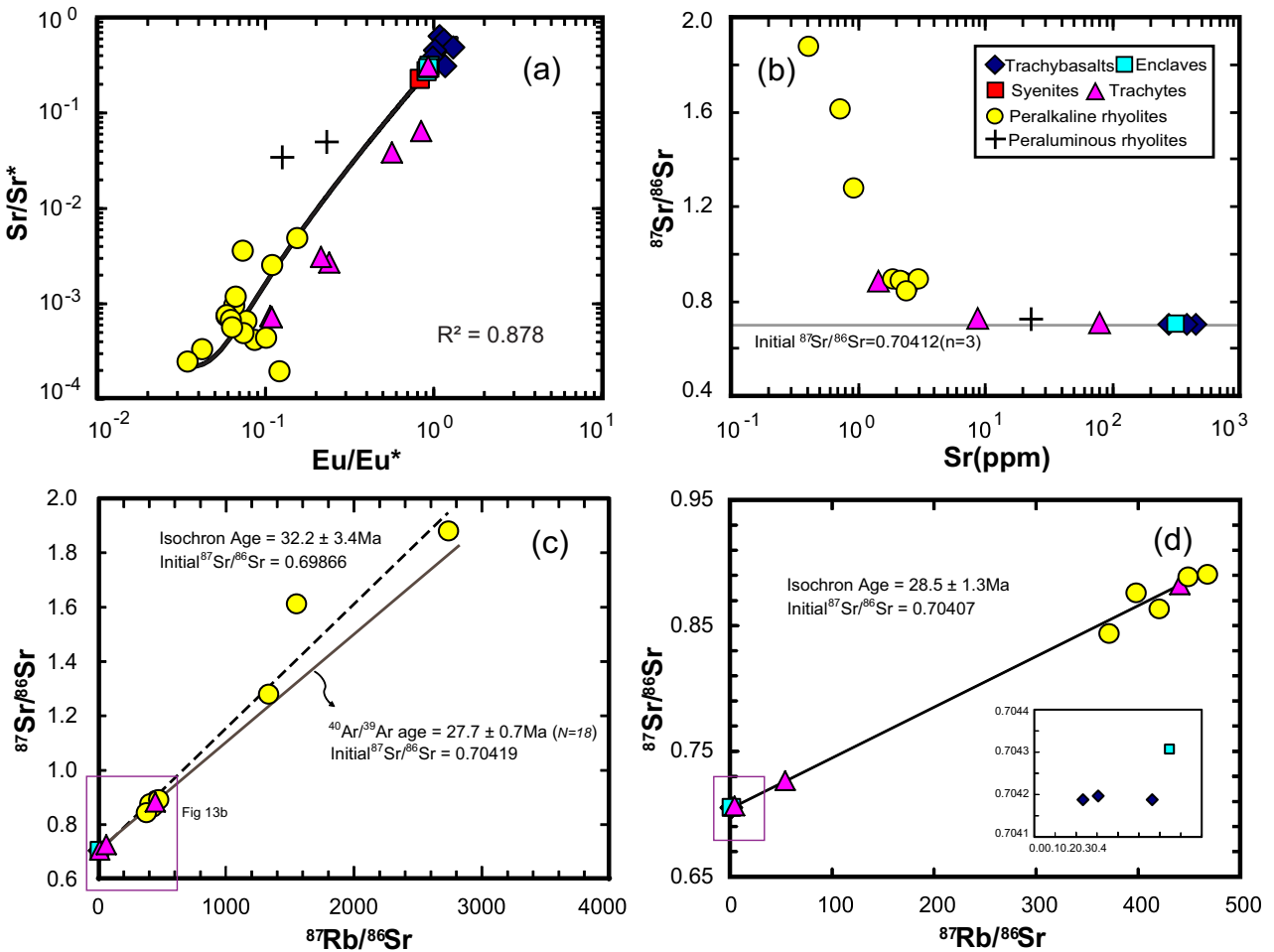


Fig. 6. (a) Correlated Eu/Eu* vs. Sr/Sr* variation, indicating that both parameters are controlled by a common process involving fractional crystallization of plagioclase (Niu and O'Hara, 2009) and K-rich feldspars in these highly evolved rhyolites. (b) $^{87}\text{Sr}/^{86}\text{Sr}$ increases with decreasing Sr. Trachytes and peralkaline rhyolites have extremely low Sr contents and high $^{87}\text{Sr}/^{86}\text{Sr}$ ratios because almost all the Sr in these rocks are radiogenic ^{87}Sr resulting from ^{87}Rb decay. (c) Rb-Sr isotope pseudochron age defined by all the rocks of the GHM area analyzed. Note that the older ages and lower initial values than expected compared to the $^{40}\text{Ar}/^{39}\text{Ar}$ ages (Cohen et al., 2007) are mainly due to three comendites with $^{87}\text{Sr}/^{86}\text{Sr} > 1$ and huge $^{87}\text{Sr}/^{86}\text{Sr}$ (with greater analytical uncertainties). (d) Excluding the three anomalously high $^{87}\text{Sr}/^{86}\text{Sr}$ comendite samples in (c), the new Rb-Sr isotope pseudochron (28.2 Ma) coincides with the Ar-Ar ages (26.4 Ma–31.0 Ma) and the initial $^{87}\text{Sr}/^{86}\text{Sr}$ ratio (0.70407) sufficiently similar to 0.70412 of the trachybasalts. Also see Figs. S4 and S5.

known phase that can simultaneously and effectively fractionate Eu and Sr from other elements (see Niu and O'Hara, 2009), resulting in the significant depletion of Eu and Sr characteristic of peralkaline rhyolites. Crystallization of alkali feldspar at the trachyte stage and thereafter will facilitate the Eu and Sr depletion in the residual melt (see above).

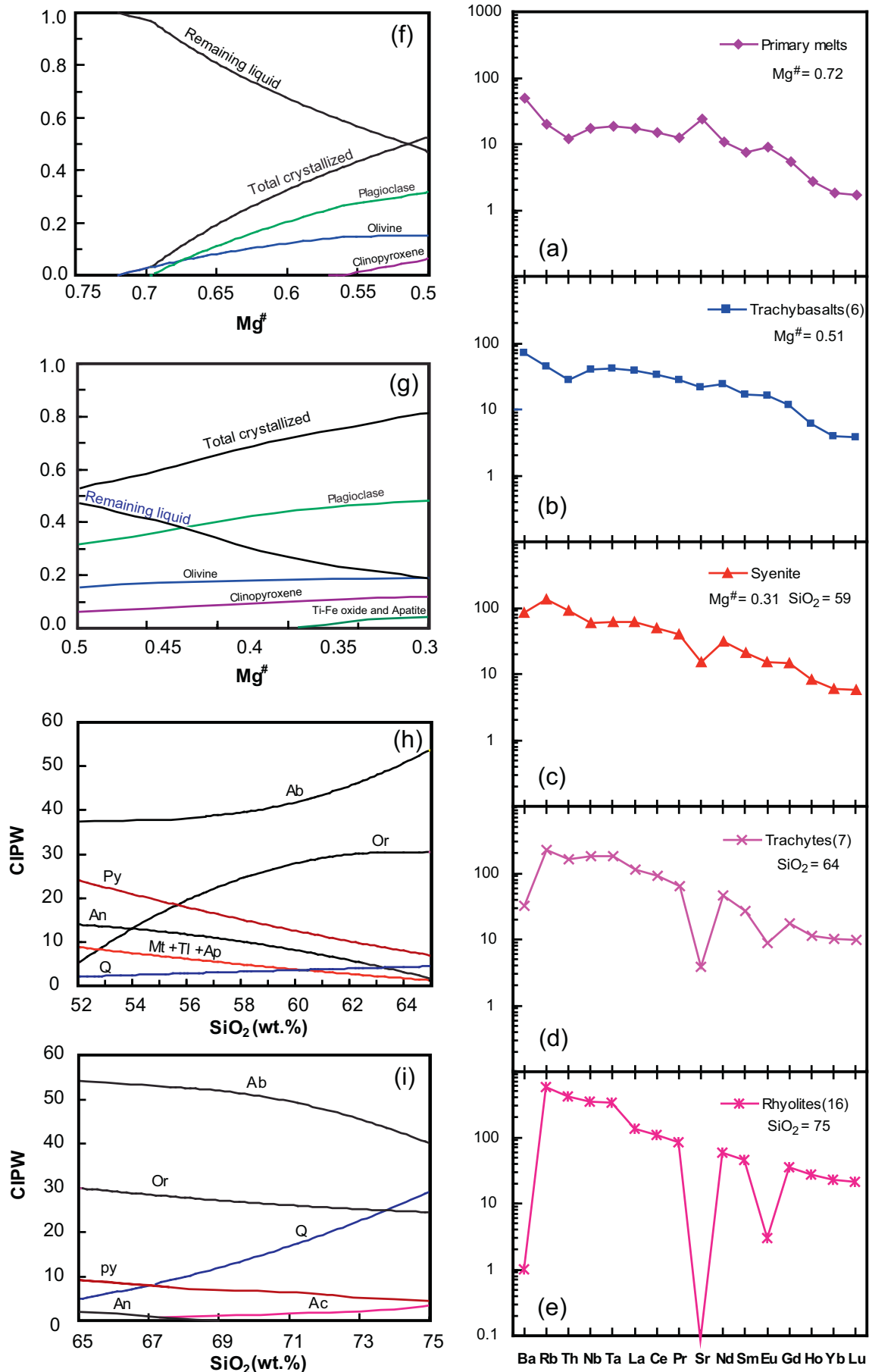
6.3.3. Effect of plagioclase crystallization on Rb/Sr and ultimately on $^{87}\text{Sr}/^{86}\text{Sr}$

The variably high $^{87}\text{Sr}/^{86}\text{Sr}$ isotope ratios of trachytes and peralkaline rhyolites (Fig. 6b–d) are often considered unlikely or analytically in error, but as discussed above these values are in fact straightforward consequences of plagioclase (to a lesser extent K-feldspar also) crystallization which depletes Sr (Figs. S4a, S5) and thus raises Rb/Sr (Fig. S4a), resulting in elevated $^{87}\text{Sr}/^{86}\text{Sr}$ in the trachytes and peralkaline rhyolites (Figs. 6b–d, S5b, d; Halliday et al., 1991). That is, at the time of magma

solidification, the trachytes and especially the peralkaline rhyolites have essentially no Sr, and the present-day measured Sr in these rocks is almost entirely radiogenic ^{87}Sr , and thus gives “unexpectedly” high $^{87}\text{Sr}/^{86}\text{Sr}$ ratios in these rocks. Note that exceedingly low Sr concentrations of the peralkaline rhyolites (0.4 ppm) are inconsistent with post-fractionation crustal contamination. Crustal contamination cannot be responsible for the very low Sr content (Halliday et al., 1989).

The above illustrative interpretation is readily confirmed by the $^{87}\text{Sr}/^{86}\text{Sr}$ – $^{87}\text{Rb}/^{86}\text{Sr}$ isochron age of 28.2 Ma with an initial $^{87}\text{Sr}/^{86}\text{Sr}$ ratio of 0.70407 defined by trachybasalts, trachytes and peralkaline rhyolites (Fig. 6d), which is essentially the same as the mean Ar–Ar age of these rocks (average age = 27.7 Ma, n = 18, Cohen et al., 2007). The coincidence of the isochron age and the mean Ar–Ar age is convincing evidence for the allied petrogenetic relationship of these different rock types in the GHM area.

Fig. 7. Trace element abundances (normalized to primitive mantle values of Sun and McDonough, 1989) in residual melt as a result of extended extent of fractional crystallization from alkali basalts through to the highly evolved peralkaline rhyolites. (a) Estimated primitive alkali basalt melt composition (see text). (b), (c), (d) and (e) are, respectively, average compositions of trachybasalt (n = 6), syenite (n = 1), trachyte (n = 7) and peralkaline rhyolite (n = 16) of the GHM samples. Panels on the left illustrate mass fractions of minerals crystallized and residual melt left as a function of decreasing Mg[#] (= Mg/Mg + Fe²⁺) for basalts (f and g) and increasing SiO₂ for the more evolved melts (h and i). For the latter, CIPW normative mineralogy is used for approximation because of lacking liquid lines of descent codes for such extreme extent of fractionation. Crystallization of (a) through mineral assemblage in (f) can produce the melt in (b), which crystallizes through mineral assemblage of (g) to produce melt of (c). The same principle to the other panels. Note that the peralkaline characteristics are developed relatively late at the time of trachyte formation and afterwards with continued crystallization of plagioclase and K-feldspars for the Ba, Sr (also P and Ti, not shown) depletion, but the high Nb and Ta are inherited from the alkali basalt parents (see Fig. 5 above).



6.4. Summary of fractional crystallization

Fig. 7 summarizes our fractional crystallization interpretation for the petrogenesis of the peralkaline rhyolites from the trachybasalts. **Fig. 7a** shows that the estimated primitive alkali basalt melt composition ($Mg^{\#} = 0.72$, estimated near primary average composition of Hawaii ocean island basalts; Dasgupta et al., 2010) evolves to an average composition of trachybasalts ($n = 6$; **Fig. 7b**) through fractional crystallization and separation of olivine (32.9%), plagioclase (56.8%) and clinopyroxene (10.3%) (**Fig. 7f**) using the LLD model of Petrolog (Danyushevsky, 1998). Trace element partition coefficients used are the compilation of Niu et al. (1996). Continued fractional crystallization (**Fig. 7g**) leads to the melt composition equivalent to the syenite (**Fig. 7c**).

At $Mg^{\#} = \sim 0.37$ in the melt, Ti–Fe oxides and apatite began to crystallize (**Fig. 7g**). Because Ti–Fe oxides contain little SiO_2 , their crystallization leads to rapid increase of SiO_2 in the residual melt. Consequently, the system produces abundant basalts and the more evolved trachytes and peralkaline rhyolites with limited volumes of intermediate rocks, i.e., the observed “Daly Gap” (see discussion in Niu et al., 2013). Because the partition coefficient $Kd_{Nb,Ta}/Kd_{Th,U} > 1$ in the ilmenite, the evolved trachytes and peralkaline rhyolites are expected to have slightly lower Nb/Th and Ta/U than in the trachybasalts (**Fig. 5a**). Furthermore, in the protracted fractionation processes with $D_{Nb}/D_{Ta} < 1$ (Niu and Batiza, 1997), it is anticipated that the highly evolved trachytes and peralkaline rhyolites have higher Nb/Ta than the parental trachybasalts (**Fig. 5b**).

After a large amount of plagioclase separation (**Fig. 7f–i**), the positive Sr and Eu anomalies in the primitive mantle melts (Niu and O’Hara, 2009) gradually disappear and the more evolved syenite, trachytes, and peralkaline rhyolites become progressively and highly depleted in Ba, Sr and Eu with strongly developed negative anomalies (**Figs. 4, S5**). Crystallization of Ca-rich plagioclase plays the key role to produce peralkaline magmas with $[Na + K]/Al > 1$. Continued crystallization of plagioclase and K-rich feldspar can produce the residual melt with striking Sr and Eu depletion ($Sr/Sr^* \ll 1$ and $Eu/Eu^* \ll 1$; **Fig. S5**), and elevated Rb/Sr ratio (**Fig. S4a**), and hence the elevated radiogenic $^{87}Sr/^{86}Sr$ in the trachytes and peralkaline rhyolites (**Figs. 6, S5b, d**).

Note that the CIPW normative mineralogy in **Fig. 7h** approximates the “ideal” liquidus phases during the melt evolution with syenite composition to the trachytes (**Fig. 7d**), and the CIPW normative mineralogy in **Fig. 7i** approximates the “ideal” liquidus phases during the trachyte melt evolution to the peralkaline rhyolites (**Fig. 7e**). The appearance of normative acmite (ac; $[Na, Fe][Si_2O_6]$; **Fig. 7i**) approximates the melt of peralkaline composition with actual mineral phases being quench crystals of sanidine–‘anorthoclase’, quartz, arfvedsonite and aegirine in the rocks. The total extent of fractional crystallization from the trachybasalts to the peralkaline rhyolites is 85% to 95% (i.e., with a residual liquid fraction of 0.5–0.15) as approximated by the Rayleigh fractionation of plagioclase on the effect of Sr and Rb/Sr (**Fig. S4a**).

Note that we attempted to use thermodynamic modeling by using the MELTS models (i.e., MELTS, pMELTS and rhyolite-MELTS), but did not succeed in doing so because these models are not yet applicable for producing peralkaline rhyolite melts (i.e., lacking data on alkaline minerals like aegirine, arfvedsonite etc.; personal communication with Professor Mark Ghiorso who is the developer of these models). Further thermodynamic development is needed for modeling the peralkaline rhyolite petrogenesis.

6.5. Melting of crustal rocks of basaltic composition will not produce peralkaline rhyolites

While melting of old crustal rocks of mafic compositions has been proposed as a method to produce peralkaline rhyolites (e.g., Bohrson and Reid, 1997 and Lowenstein and Mahood, 1991), we consider that

this is unlikely an effective mechanism for peralkaline rhyolites in explaining all the petrological and geochemical characteristics demonstrated above. Furthermore, Fig. S6 shows in simple clarity that melting of basaltic rocks cannot even explain the Zr–Ni in the GHM rock suites. Trace element is depleted much more rapidly during fractional crystallization than melting when the bulk partition coefficient is greater than 1. Even assuming a high D_{Ni} , it is hardly possible to achieve such low Ni concentrations of the peralkaline rhyolites through equilibrium batch melting.

6.6. Origin of the peraluminous rhyolites

The peraluminous rhyolites (samples LGN-7 and LGN-9A) are best interpreted as resulting from crustal anatexis in response to underplating of alkali-rich basaltic magmas (parental to the trachybasalts) of the same thermal event of ~ 28 Ma. The same initial Sr and Nd isotopes of these peraluminous rhyolites and all other rocks (**Figs. 6b, S4b**) imply the possibility that the source rocks of the peraluminous rhyolites may be related to the underplated basaltic rocks (could be cumulate), whose partial melting under amphibolite facies conditions can readily explain both major element and trace element characteristics of the peraluminous rhyolites (see Niu and O’Hara, 2009). This possibility can be tested in the future.

7. Conclusions

- (1) The peralkaline rhyolites of the GHM area are characterized by high Nb (vs. Th) and Ta (vs. U), extreme depletion of Ba, Sr, and Eu and variably very high $^{87}Sr/^{86}Sr$.
- (2) All these features are most consistent with protracted fractional crystallization of alkali basalts (parental to the trachybasalts). The high abundances of Nb and Ta and especially the high Nb/Ta ratios are inherited from the inferred alkali basalt parent. Plagioclase (and K-feldspar) crystallization depletes Ba, Sr and Eu in the residual melts with Sr/Sr^* and Eu/Eu^* values approaching nil. The extremely low Sr and thus the high Rb/Sr ratio explain that essentially all of the Sr in the peralkaline rhyolites is radiogenic ^{87}Sr accumulated from ^{87}Rb decay since the volcanism.
- (3) The GHM rock types altogether define a $^{87}Sr/^{86}Sr - ^{87}Rb/^{86}Sr$ isochron of ~ 28 Ma, which is essentially identical to the Ar–Ar ages of these rocks in the literature, demonstrating the co-evality of the GHM rocks and the validity of our petrogenetic interpretation of the peralkaline rhyolite petrogenesis.
- (4) Major and trace element molding of the fractionation processes shows that the total extent of fractional crystallization from the trachybasalts to the peralkaline rhyolites is 85% to 95%.
- (5) The petrogenesis of the common peraluminous rhyolites is consistent with crustal anatexis probably induced by underplated basaltic melts equivalent to the melts parental to the trachybasalts of the same mantle plume/hotspot magmatic event at ~ 28 Ma.
- (6) We suggest that our interpretation of the petrogenesis of peralkaline rhyolites may be of general significance globally, but further tests are needed.

Acknowledgments

The research was supported by Australian ARC grants and Chinese NSF grants (91014003, 41130314) to Yaoling Niu. We thank Alan Grieg, Fiona Lenkite and Immo Wendt for field and laboratory assistance. We thank Dr. Sutherland and the anonymous reviewer for constructive comments.

Appendix A

Appendix Table 1

Major and trace element compositions of Glass House Mountains.

Sample	LGN-10	LGN-11A	LGN-12A	LGN-13A	LGN-33	LGN-34	LGN-5A	LGN-5B	LGN-5D	LGN-5H	LGN-16B	LGN-16D	LGN-22B	LGN-23A	LGN-29	LGN-30A	LGN-31
SiO ₂	50.1	50.1	49.8	51.3	48.8	52.5	59.4	52.3	51.8	53.5	65.9	66.8	61.6	62.7	61.5	63.6	64.3
TiO ₂	1.46	2.52	2.41	2.42	2.74	2.01	1.31	2.48	2.58	2.63	0.12	0.10	0.31	0.42	0.45	0.23	0.19
Al ₂ O ₃	15.0	15.3	14.9	15.6	15.6	15.4	15.1	14.1	14.1	14.5	16.7	16.3	17.1	16.5	17.3	16.1	16.6
FeOt	10.5	9.78	10.2	10.2	11.2	10.1	7.19	10.2	10.5	10.5	3.43	3.37	5.64	4.56	5.24	5.16	4.55
MnO	0.13	0.14	0.21	0.13	0.15	0.16	0.12	0.19	0.19	0.21	0.08	0.07	0.17	0.16	0.12	0.20	0.11
MgO	6.65	4.75	4.55	4.95	4.24	5.29	1.52	2.97	3.00	3.00	0.03	0.05	0.35	0.29	0.35	0.11	0.10
CaO	7.51	8.05	7.52	6.96	6.67	5.92	3.72	6.21	5.77	5.54	0.36	0.29	2.05	1.76	2.32	1.44	1.34
Na ₂ O	3.27	3.61	3.66	3.91	3.95	3.80	4.48	4.65	4.75	5.09	6.80	6.97	5.26	5.48	5.40	6.00	6.18
K ₂ O	0.72	1.46	1.72	1.85	1.96	2.14	3.24	1.17	1.10	1.44	4.56	4.57	5.58	5.36	5.50	5.46	5.52
P ₂ O ₅	-	0.50	0.64	0.58	1.03	0.68	0.43	0.52	0.51	0.52	-	-	0.17	0.13	0.10	-	0.03
LOI	4.52	3.39	3.52	1.86	2.48	1.70	2.05	3.40	3.99	1.21	0.84	0.64	1.94	1.66	1.43	1.03	1.19
Total	99.8	99.6	99.1	99.7	98.8	99.7	98.5	98.2	98.2	98.1	98.7	99.17	100	99.0	99.7	99.3	100
Mg [#]	0.57	0.50	0.48	0.50	0.44	0.52	0.31	0.38	0.38	0.38	0.02	0.03	0.12	0.12	0.12	0.04	0.04
Pl	0.41	0.49	0.53	0.54	0.55	0.56	0.72	0.64	0.64	0.69	0.97	1.01	0.86	0.90	0.86	0.98	0.97
Li	5.87	4.14	2.94	7.45	11.6	9.50	23.7	36.7	39.2	26.6	65.0	69.3	38.5	17.7	21.3	43.1	48.0
Be	0.65	1.18	1.09	1.82	1.98	1.86	2.93	2.16	2.11	2.04	7.70	4.82	2.22	3.63	4.35	10.2	9.99
Sc	16.8	15.4	16.2	14.9	12.9	16.9	10.5	16.6	16.4	17.2	0.56	0.49	16.5	5.93	9.17	4.59	2.99
V	136	134	137	133	130	93.4	46.4	159	154	166	-	-	156	1.72	0.45	0.05	0.13
Cr	229	72.9	105	85.8	36.5	132	41.8	31.7	30.6	50.9	8.71	7.77	36.6	36.2	21.8	-	13.8
Co	45.7	40.0	39.7	34.9	36.9	31.1	11.3	26.9	25.8	26.5	0.11	0.08	27.4	1.84	1.70	0.65	0.47
Ni	149	79.9	86.5	63.0	36.2	83.5	4.26	8.08	10.5	11.7	0.35	0.43	11.1	1.39	1.50	0.77	0.92
Cu	37.4	35.5	36.0	51.7	40.8	38.1	13.3	37.1	30.3	40.6	4.81	4.93	35.5	9.09	11.1	10.7	9.72
Zn	99.1	115	113	120	134	123	84.5	173	147	167	187	221	171	116	116	208	161
Ga	19.1	22.9	22.0	24.3	25.5	24.4	26.0	25.3	25.1	25.3	53.3	53.9	24.4	35.0	33.2	43.4	42.9
Rb	14.6	22.1	18.4	36.6	34.1	37.1	84.3	39.2	35.7	44.1	221	225	39.0	92.9	89.2	145	161
Sr	276	512	457	507	523	381	310	356	320	360	1.45	1.18	354	79.6	115	8.24	8.77
Y	16.3	21.5	22.1	25.4	29.3	27.3	32.7	28.6	29.1	30.8	45.0	25.1	28.5	41.4	40.6	75.5	67.4
Zr	89.3	179	173	244	266	268	321	273	272	270	1088	1129	268	600	709	1190	991
Nb	10.2	24.6	23.6	33.3	40.4	34.5	41.1	37.1	37.3	41.8	208	214	36.1	67.9	69.9	138	147
Sn	1.08	1.76	1.67	2.27	2.27	2.36	5.10	3.63	3.64	3.28	15.6	17.3	3.61	5.10	5.45	11.2	11.9
Cs	0.43	0.17	0.27	0.20	0.14	0.25	1.55	1.96	1.42	1.25	0.60	0.23	1.96	0.38	0.90	0.31	0.93
Ba	165	372	689	423	469	808	582	266	248	349	3.30	1.31	264	453	766	48.2	58.3
La	9.87	22.4	23.2	30.6	36.6	32.8	41.5	32.8	33.3	34.6	85.7	74.5	32.7	76.9	60.3	108	104
Ce	22.7	50.2	51.8	66.8	80.0	72.4	87.6	70.5	71.4	74.4	267	70.6	69.9	152	123	221	212
Pr	3.16	6.67	6.96	8.62	10.4	9.42	10.9	8.89	9.11	9.49	18.2	15.0	8.93	17.5	14.6	25.6	24.3
Nd	13.8	28.0	29.6	34.9	42.9	38.2	41.9	35.4	36.3	38.0	55.6	46.7	35.6	61.9	53.7	92.0	84.3
Sm	3.70	6.57	6.84	7.85	9.58	8.41	9.21	8.04	8.28	8.67	10.2	8.02	8.10	11.6	10.9	18.5	16.8
Eu	1.38	2.45	2.93	2.58	3.05	3.16	2.46	2.48	2.45	2.63	0.34	0.26	2.45	2.04	2.88	1.40	1.12
Gd	4.04	6.28	6.69	7.40	8.99	7.86	8.67	7.76	7.97	8.38	8.59	6.15	7.84	10.0	9.59	16.5	14.7
Tb	0.60	0.88	0.91	1.02	1.21	1.09	1.22	1.10	1.12	1.17	1.53	0.94	1.09	1.45	1.41	2.46	2.24
Dy	3.57	4.88	4.99	5.65	6.64	6.13	7.00	6.19	6.34	6.65	9.88	5.50	6.25	8.43	8.34	14.6	13.4
Ho	0.68	0.88	0.90	1.03	1.21	1.12	1.32	1.14	1.17	1.24	1.97	1.05	1.16	1.63	1.62	2.85	2.63
Er	1.77	2.24	2.26	2.64	3.05	2.85	3.49	2.98	3.05	3.23	5.68	3.14	3.02	4.54	4.47	8.05	7.41
Tm	0.24	0.30	0.29	0.35	0.40	0.38	0.47	0.40	0.41	0.43	0.91	0.52	0.40	0.66	0.64	1.16	1.07
Yb	1.45	1.74	1.68	2.06	2.30	2.24	2.85	2.37	2.44	2.59	6.06	3.87	2.39	4.22	4.06	7.25	6.83
Lu	0.21	0.25	0.24	0.29	0.33	0.32	0.41	0.33	0.35	0.37	0.87	0.60	0.34	0.65	0.61	1.08	1.02
Hf	2.35	4.35	4.16	5.83	6.40	6.24	7.84	6.56	6.67	6.54	28.5	29.6	6.57	12.7	15.1	25.8	24.2
Ta	0.63	1.48	1.43	2.01	2.46	2.03	2.47	2.19	2.28	2.50	12.3	13.2	2.21	3.84	3.94	7.49	8.35
Pb	1.61	2.16	2.07	3.59	3.47	3.85	6.19	6.08	4.67	25.1	26.8	12.4	6.36	8.83	10.8	17.7	18.2
Th	1.18	1.87	2.09	3.03	2.88	2.76	7.55	4.69	4.94	4.69	24.9	25.2	4.64	8.69	6.82	12.7	14.0
U	0.35	0.52	0.55	0.92	0.89	0.84	2.09	1.38	1.44	1.32	5.01	3.11	1.35	2.44	2.12	3.90	4.35
Ce/Ce*	0.99	1.00	0.99	0.99	1.00	0.99	0.99	0.99	0.99	0.99	1.58	0.49	0.98	0.98	0.99	0.99	1.00
Sr/Sr*	0.64	0.58	0.49	0.45	0.38	0.31	0.23	0.31	0.27	0.29	0.001	0.001	0.31	0.04	0.06	0.003	0.003
Eu/Eu*	1.08	1.15	1.31	1.02	0.99	1.17	0.83	0.95	0.91	0.93	0.11	0.11	0.93	0.57	0.84	0.24	0.21

Mg[#] = m. [Mg²⁺/(Mg²⁺ + Fe²⁺)], FeOt represents total iron. m. [Fe²⁺/(Fe²⁺ + Fe³⁺)] = 0.85, Pl = m. [(Na₂O + K₂O)/Al₂O₃], Eu/Eu* = w(Eu)_N/[w(Sm)_N + w(Gd)_N], Ce/Ce* = w(Ce)_N/[w(La)_N + w(Pr)_N], subscript N represents chondrite normalized (Sun and McDonough, 1989). Sr/Sr* (= 2^{sr}_{PM}/[Pr_{PM} + Nd_{PM}]).

Appendix Table 1 (continued)

Sample	LGN-3A	LGN-4A	LGN-8C	LGN-14	LGN-15	LGN-18A	LGN-20A	LGN-20D	LGN-19A	LGN-21A	LGN-24A	LGN-25A	LGN-28	LGN-27	LGN-26C	LGN-7	LGN-9A
SiO ₂	74.7	75.1	75.6	74.8	73.7	75.5	74.4	75.6	75.4	73.9	72.6	74.0	70.6	71.3	73.8	74.5	75.3
TiO ₂	0.13	0.12	0.13	0.08	0.19	0.10	0.11	0.12	0.13	0.12	0.14	0.11	0.10	0.18	0.13	0.07	0.13
Al ₂ O ₃	11.8	11.8	11.7	12.6	11.0	11.8	11.5	12.0	11.3	13.4	13.3	11.4	14.6	13.5	13.5	12.6	13.1
FeOt	2.82	2.85	2.85	2.20	4.37	2.77	3.00	3.02	3.57	2.22	3.11	2.97	3.03	3.95	2.24	1.54	0.72
MnO	0.03	0.03	0.03	0.03	0.06	0.04	0.05	0.06	0.07	0.02	0.05	0.04	0.07	0.07	0.03	0.05	—
MgO	0.01	0.02	0.04	0.03	0.04	0.01	0.03	0.06	0.03	0.04	0.02	0.12	0.03	0.03	0.08	0.20	0.25
CaO	0.05	0.03	0.06	0.04	0.16	0.05	0.09	0.03	0.08	0.05	0.22	0.04	0.27	0.09	0.09	0.45	0.56
Na ₂ O	4.74	4.74	4.35	4.74	4.59	4.95	5.16	4.81	4.92	5.07	5.69	4.58	6.37	4.93	4.78	3.13	3.29
K ₂ O	4.30	4.07	4.33	3.98	4.10	4.12	3.97	4.03	3.88	4.40	4.29	4.16	4.45	4.60	4.58	4.58	4.86
P ₂ O ₅	0.10	0.10	0.11	—	0.02	0.04	0.02	0.02	0.04	—	0.02	—	—	—	—	0.11	0.10
LOI	0.46	0.58	0.61	0.75	0.55	0.30	0.36	0.25	0.55	0.93	0.37	1.36	0.69	1.72	1.40	1.89	1.39
Total	99.1	99.4	99.8	99.2	98.8	99.7	98.7	99.9	100	100	99.8	98.8	100	100	101	99.0	99.7
Mg [#]	0.01	0.01	0.03	0.03	0.02	0.01	0.02	0.04	0.02	0.03	0.02	0.08	0.02	0.01	0.07	0.21	0.42
Pl	1.06	1.04	1.01	0.97	1.09	1.07	1.11	1.03	1.09	0.98	1.05	1.06	1.05	0.98	0.95	0.81	0.82
Li	126	165	109	97.0	98.2	113	138	131	115	82.0	96.3	130	134	99.2	91.5	97.8	64.1
Be	9.08	23.3	16.3	8.42	10.7	17.7	25.0	21.4	21.0	12.7	17.6	24.2	23.8	14.2	6.93	7.27	5.67
Sc	0.58	0.58	0.71	3.09	1.00	0.51	0.71	0.63	1.40	0.56	0.58	0.66	0.48	0.89	0.76	1.81	2.00
V	—	—	0.05	—	0.14	—	0.15	—	—	0.01	—	0.03	0.14	0.30	0.02	0.99	3.91
Cr	0.03	0.17	0.84	19.3	21.5	31.7	75.6	0.11	0.31	6.40	0.16	0.15	22.9	0.01	0.09	21.5	2.56
Co	0.03	0.02	0.08	0.08	0.04	0.10	0.21	0.05	0.19	—	0.20	—	0.04	0.36	0.09	0.76	0.76
Ni	0.46	0.23	0.51	0.60	0.95	0.86	1.65	0.17	0.21	0.85	0.99	0.47	1.17	0.50	0.65	0.80	1.96
Cu	4.06	4.81	5.11	4.25	4.06	2.69	2.80	2.60	2.85	4.55	2.13	3.08	6.04	3.90	2.63	1.58	4.96
Zn	318	426	292	253	279	284	357	320	354	181	286	357	379	253	198	54.5	32.7
Ga	53.8	60.4	49.7	50.1	53.9	52.2	60.5	59.2	61.9	52.2	60.3	61.9	65.7	59.3	51.9	26.5	23.7
Rb	392	533	426	343	292	392	492	445	359	315	327	484	357	317	312	256	229
Sr	0.73	0.72	0.93	2.57	1.89	0.41	4.12	1.66	2.47	2.29	2.07	3.00	2.27	0.54	2.44	23.5	37.8
Y	71.5	219	94.7	52.9	193	45.5	168	103	119	122	147	251	141	77.2	70.0	49.7	31.9
Zr	1120	1354	1199	494	2165	1191	1780	1648	2122	805	1343	1715	983	1625	861	84.9	93.6
Nb	71.7	253	191	205	276	229	377	318	357	205	267	347	359	276	217	44.3	25.3
Sn	17.0	32.8	28.1	24.2	24.3	26.8	39.6	34.7	32.1	20.4	25.3	39.8	33.9	25.8	21.1	12.9	9.35
Cs	1.15	6.45	5.64	3.21	0.54	5.04	7.55	3.51	1.76	1.92	4.98	2.16	2.29	3.18	0.75	8.77	6.14
Ba	1.04	1.27	3.76	4.12	4.66	2.04	5.63	5.05	14.0	4.58	7.23	7.46	4.55	3.47	40.7	135	209
La	66.8	75.7	34.8	32.3	397	27.6	118	62.0	19.9	193	91.6	165	116	40.5	16.9	24.3	29.4
Ce	89.0	163	128	64.6	696	89.9	174	122	184	424	200	185	266	137	39.7	50.0	58.1
Pr	18.6	23.4	12.3	6.74	84.3	8.62	35.5	12.7	7.48	41.4	23.7	37.7	33.1	10.9	4.32	5.86	6.67
Nd	65.8	89.7	41.7	20.5	286	29.4	131	40.8	30.6	137	84.1	134	122	36.3	14.8	20.8	23.0
Sm	17.5	30.2	13.8	4.70	53.8	7.98	38.8	11.6	14.1	27.5	21.6	35.8	29.6	9.61	4.13	5.76	5.44
Eu	0.23	0.38	0.38	0.12	1.97	0.22	0.83	0.26	0.57	0.64	0.43	0.77	0.61	0.33	0.25	0.26	0.42
Gd	15.9	37.6	16.3	5.52	43.0	7.35	38.4	12.6	18.1	24.2	23.0	39.0	28.9	10.4	5.81	6.84	5.40
Tb	2.66	6.64	3.10	1.34	6.36	1.42	6.22	2.86	3.62	3.90	4.02	6.62	4.61	2.07	1.44	1.26	0.92
Dy	15.3	40.7	19.9	10.1	37.6	9.43	35.8	20.9	24.2	23.2	25.9	41.6	27.1	14.0	11.4	8.30	5.73
Ho	2.81	7.94	3.98	2.13	7.41	1.92	6.56	4.37	4.88	4.37	5.21	8.17	5.08	2.94	2.61	1.70	1.14
Er	7.45	21.1	11.4	6.39	21.1	5.85	17.4	13.2	14.0	11.7	14.8	21.3	13.5	8.74	8.05	4.81	3.21
Tm	1.12	3.06	1.84	1.04	3.00	0.97	2.49	2.11	2.17	1.61	2.18	2.87	1.86	1.42	1.29	0.74	0.48
Yb	7.27	18.3	12.1	6.67	18.0	6.61	15.2	13.6	14.0	9.28	13.0	16.7	11.1	9.62	8.14	4.64	3.05
Lu	1.05	2.49	1.71	0.87	2.54	0.94	1.99	1.86	1.93	1.24	1.74	2.30	1.49	1.45	1.15	0.64	0.42
Hf	36.0	45.7	37.3	21.0	50.7	36.0	54.6	48.3	56.0	25.5	38.0	56.4	36.4	44.2	27.1	4.41	4.22
Ta	3.82	14.6	9.93	14.7	13.2	13.3	21.8	15.1	20.1	9.45	14.0	21.7	18.7	14.4	10.5	3.89	2.74
Pb	26.0	62.3	45.3	39.7	21.8	41.5	53.1	47.9	82.4	35.6	31.4	26.0	44.0	32.7	36.2	20.5	22.7
Th	36.7	48.8	45.8	25.4	35.4	34.1	48.7	43.9	44.1	26.3	32.7	31.6	33.1	36.6	28.9	24.4	22.9
U	3.26	15.0	11.9	6.11	10.3	7.84	13.3	8.76	7.79	5.51	9.27	12.3	7.19	5.82	5.07	4.10	5.63
Ce/Ce*	0.61	0.94	1.52	1.02	0.89	1.42	0.65	1.01	3.69	1.11	1.03	0.55	1.04	1.57	1.11	0.99	0.98
Sr/Sr*	0.0003	0.0002	0.0007	0.004	0.0002	0.0004	0.003	0.001	0.001	0.0005	0.0007	0.0007	0.005	0.0004	0.0006	0.03	0.05
Eu/Eu*	0.04	0.03	0.08	0.07	0.12	0.09	0.07	0.07	0.11	0.07	0.06	0.06	0.06	0.10	0.15	0.13	0.23

Appendix Table 2

Blank levels and USGS reference standards BIR-1 and AGV-1 analyzed by ICP-MS at the University of Queensland.

	AGV-1 (ppm)	RSD (%)	BIR-1 (ppm)	RSD (%)	Blank (ppb)	1σ
Li	12.1	5.4	3.11	2.7	0.056	0.040
Be	2.20	4.7	0.09	8.8	0.019	0.028
Sc	12.4	3.4	43.5	1.6	2.071	2.547
V	111	1.8	283	3.5	0.088	0.087
Cr	8.7	5.5	373	3.1	0.755	0.786
Co	16.0	2.7	55	7.1	0.239	0.193
Ni	16.6	4.6	170	2.1	2.156	1.175
Cu	62.5	2.0	121	2.2	0.229	0.100
Zn	81.9	3.0	66.0	3.9	2.058	0.855
Ga	20.3	2.4	15.4	2.3	0.074	0.094
Rb	66.6	1.8	0.20	4.4	0.044	0.031
Sr	646	1.8	109	1.3	1.240	2.187
Y	17.4	2.1	13.5	2.4	0.003	0.001
Zr	211	1.7	13.1	2.0	0.007	0.003
Nb	14.2	1.6	0.54	1.2	0.008	0.005
Cs	1.26	2.4	0.005	9.9	0.005	0.003
Ba	1162	2.8	6.44	2.1	0.035	0.016
La	37.6	2.2	0.58	3.4	0.004	0.001
Ce	67.2	2.3	1.84	1.7	0.004	0.002
Pr	8.71	2.1	0.38	1.8	0.003	0.001
Nd	30.2	2.5	2.24	1.7	0.007	0.002
Sm	5.44	2.2	1.02	1.5	0.017	0.009
Eu	1.54	5.4	0.49	1.7	0.003	0.001
Gd	5.16	4.1	1.67	3.2	0.011	0.003
Tb	0.61	3.0	0.32	2.6	0.001	0.000
Dy	3.37	2.6	2.38	2.2	0.006	0.002
Ho	0.64	2.4	0.52	2.4	0.002	0.001
Er	1.79	2.3	1.54	2.5	0.004	0.001
Tm	0.23	2.2	0.22	2.1	0.001	0.000
Yb	1.54	1.8	1.49	2.8	0.004	0.001
Lu	0.23	2.6	0.22	2.1	0.001	0.000
Hf	4.91	2.0	0.53	1.8	0.005	0.001
Ta	0.84	2.4	0.05	1.1	0.003	0.001
Pb	32.5	0.8	2.81	3.1	0.015	0.005
Th	5.90	2.1	0.03	6.6	0.002	0.000
U	1.88	1.9	0.01	4.4	0.005	0.011

Appendix Table 3

Sr, Nd and Pb isotope data for selected volcanic rocks from Glass House Mountains.

Sample	$^{87}\text{Sr}/^{86}\text{Sr}$	$^{143}\text{Nd}/^{144}\text{Nd}$	$\varepsilon_{\text{Nd}}(\text{t})$	$^{206}\text{Pb}/^{204}\text{Pb}$	$^{207}\text{Pb}/^{204}\text{Pb}$	$^{208}\text{Pb}/^{204}\text{Pb}$
LGN-10	0.704197	0.512582	-0.97	18.11	15.52	38.99
LGN-12A	0.704188	0.512611	-0.32	18.04	15.51	37.97
LGN-34	0.704188			17.93	15.52	37.86
LGN-5D	0.704307	0.512624	-0.07	18.33	15.56	38.27
LGN-16B	0.882093	0.512549	-1.44			
LGN-23A	0.705637	0.512604	-0.38	18.10	15.54	38.09
LGN-31	0.725749			18.09	15.59	38.07
LGN-3A	1.608921	0.512618	-0.27	18.51	15.65	38.54
LGN-8C	1.278132	0.512588	-0.99	18.55	15.62	38.63
LGN-15	0.888457			18.04	15.55	38.08
LGN-18A	1.876691			18.31	15.63	38.40
LGN-19A	0.862758	0.512612	-0.79	18.37	15.66	38.51
LGN-20D				18.10	15.53	38.06
LGN-21A	0.875652			18.39	15.77	38.72
LGN-25A	0.890399	0.51261	-0.43	18.15	15.60	38.29
LGN-26C	0.843217	0.512576	-1.12	18.23	15.60	38.27
LGN-7	0.718565	0.512625	-0.16	18.50	15.61	38.55

Pb isotope compositions are calculated at 28 Ma.

Appendix B. Supplementary data

Supplementary data to this article can be found online at <http://dx.doi.org/10.1016/j.lithos.2014.12.015>.

References

- Bhushan, S.K., Rao, K.N., Vidyadharan, K.T., 2010. Petrography and geochemistry of St. Mary islands, near Malpe, Dakshina Kannada district, Karnataka. Journal of the Geological Society of India 76, 155–163.
- Black, S., Macdonald, R., Kelly, R., 1997. Crustal origin for peralkaline rhyolites from Kenya: evidence from U-series disequilibria and Th-isotope. Journal of Petrology 38, 227–297.
- Bohrson, W.A., Reid, M.A., 1997. Genesis of silicic peralkaline volcanic rocks in an ocean island setting by crustal melting and open-system processes: Socorro Island, Mexico. Journal of Petrology 38, 1137–1166.
- Bryce, J.G., DePaolo, D.J., 2004. Pb isotopic heterogeneity in basaltic phenocrysts. Geochimica et Cosmochimica Acta 68, 4453–4468.
- Chen, X.W., 2013. Petrography and Geochemistry Indication of Crystallization Differentiation and Magma Mixing Process of the Tianchi Volcano, Changbaishan. (M.S. dissertation). Institute of Geology, China Earthquake Administration, Beijing.
- Chen, Y., Zhu, D., Zhao, Z., Meng, F., Wang, Q., Santosh, M., et al., 2014. Slab breakoff triggered ca. 113 Ma magmatism around Xainza area of the Lhasa Terrane, Tibet. Gondwana Research 26, 449–463.
- Civetta, L., Cornette, Y., Crisci, G., Gillot, P.Y., Orsi, G., Requejo, C.S., 1984. Geology, geochronology, and chemical evolution of the island of Pantelleria. Geological Magazine 121, 541–562.
- Civetta, L., D'Antonio, M., Orsi, G., Tilton, G.R., 1998. The geochemistry of volcanic rocks from Pantelleria, Sicily Channel: petrogenesis and characteristics of the mantle source region. Journal of Petrology 39, 1453–1491.
- Cohen, B.E., Knesel, K.M., Vasconcelos, P.M., Schellart, W.P., 2013. Tracking the Australian plate motion through the Cenozoic: constraints from $^{40}\text{Ar}/^{39}\text{Ar}$ geochronology. Tectonics 32, 1371–1383.
- Cohen, B.E., Vasconcelos, P.M., Knesel, K.M., 2007. $^{40}\text{Ar}/^{39}\text{Ar}$ constraints on the timing of Oligocene intraplate volcanism in southeast Queensland, Australia. Australian Journal of Earth Science 54, 105–125.
- Daly, R.A., 1925. The geology of Ascension island. Proceedings of the American Academy of Arts and Science. 60, pp. 3–123.
- Danyushevsky, L.V., 1998. The effect of small amount of H_2O on fractionation of mid-ocean ridge magmas. EOS, Transactions of the American Geophysical Union 79, 375.
- Dasgupta, R., Jackson, M.G., Lee, C.-T.A., 2010. Major element chemistry of ocean island basalts—conditions of mantle melting and heterogeneity of mantle source. Earth and Planetary Science Letters 289, 377–392.
- Ewart, A., 1982. Petrogenesis of the Tertiary anorogenic volcanic series of southern Queensland, Australia, in the light of trace element geochemistry and O, Sr and Pb isotopes. Journal of Petrology 23, 244–282.
- Ewart, A., Chappell, B.W., Menzies, M.A., 1988. An overview of the geochemical and isotopic characteristics of eastern Australian Cainozoic volcanic provinces. Journal of Petrology Special Lithosphere 1, 225–273.
- Ewart, A., Collerson, K.D., Regelous, M., Wendt, J.I., Niu, Y., 1998. Geochemical evolution within the Tonga-Kermadec-Lau Arc-Back-arc Systems: the role of varying mantle wedge composition in space and time. Journal of Petrology 39, 331–368.
- Ewart, A., Grenfell, A., 1985. Cainozoic volcanic centres in southeastern Queensland, with special reference to the Main Range, Bunya Mountains, and the volcanic centres of the northern Brisbane coastal region. Papers of the Department of Geology. 11. University of Queensland, pp. 1–57.
- Fang, N., Niu, Y., 2003. Late Paleozoic ultramafic lavas in Yunnan, SW China, and their geodynamic significance. Journal of Petrology 44, 141–158.
- Halliday, A.N., Davidson, J.P., Hildreth, W., Holden, P., 1991. Molding the petrogenesis of high Rb/Sr silicic magmas. Chemical Geology 92, 107–114.
- Halliday, A.N., Mahood, G., Holden, P., Metz, J.M., Dempster, T.J., Davidson, J.P., 1989. Evidence for long residence times of rhyolite magma in the Long Valley magma system; the isotopic record in the precaldera rhyolite lavas of Glass Mountain. Earth and Planetary Science Letters 94, 274–290.
- Heumann, A., Davies, G.R., 2002. U-Th disequilibrium and Rb-Sr age constrains on the magmatic evolution of peralkaline rhyolites from Kenya. Journal of Petrology 43, 557–577.
- Hong, W., Xu, X., Zou, H., 2013. Petrogenesis of coexisting high-silica aluminous and peralkaline rhyolite from Yunshan (Yongtai), southeastern China. Journal of Asian Earth Science 74, 316–329.
- Johnson, R.W., 1989. Intraplate Volcanism in Eastern Australia and New Zealand. Cambridge University Press, Cambridge.
- Kar, A., Weaver, B., Davidson, J., Colucci, M., 1998. Origin of differentiated volcanic and plutonic rocks from Ascension Island, South Atlantic Ocean. Journal of Petrology 39, 1009–1024.
- Knesel, K.M., Cohen, B.E., Vasconcelos, P.M., Thiede, D.S., 2008. Rapid change in drift of the Australian plate records collision with Ontong Java plateau. Nature 454, 754–757.
- Kwiecien, W., 1990. Silicate rock analysis by AAS. School of Geology, Queensland University of Technology, Brisbane.
- Le Bas, M.J., Le Maitre, R.W., Streckeisen, A., Zanettin, B., 1986. A chemical classification of volcanic rocks based on the total alkali silica diagram. Journal of Petrology 27, 745–750.
- Lowenstern, J.B., Mahood, G.A., 1991. New data on magmatic H_2O contents of pantellerites, with implications for petrogenesis and eruptive dynamics at Pantelleria. Bulletin of Volcanology 54, 78–83.
- Lustrino, M., Morra, V., Melluso, L., Brotzu, P., D'Amelio, F., Fedele, L., et al., 2004. The Cenozoic igneous activity of Sardinia. Periodico di Mineralogia 73 pp. 105–134.
- Macdonald, R., 1974. Nomenclature and petrochemistry of the peralkaline oversaturated extrusive rocks. Bulletin of Volcanology 38, 498–516.
- Macdonald, R., Bagiński, B., Ronga, F., Dzierzanowski, P., Lustrino, M., Marzoli, A., et al., 2012. Evidence for extreme fractionation of peralkaline silicic magma, the Boseti volcanic complex, Main Ethiopian Rift. Mineralogy and Petrology 104, 163–175.
- Macdonald, R., Davies, G.R., Bliss, C.M., Leat, P.T., Bailey, D.K., Smith, R.L., 1987. Geochemistry of high-silica peralkaline rhyolites, Naivasha, Kenya Rift Valley. Journal of Petrology 28, 979–1008.
- Mahood, G.A., Stiman, J.A., 1990. Trace element partitioning in pantellerites and trachytes. Geochimica et Cosmochimica Acta 54, 2257–2276.

- Marshall, A.S., Macdonald, R., Rogera, N.W., Fitton, J.G., Tindle, A.G., Nejbert, K., et al., 2009. Fractionation of peralkaline silicic magmas: the Greater Olkaria volcanic complex, Kenya Rift Valley. *Journal of Petrology* 50, 323–359.
- Mbassa, B.J., Nonfang, E., Benoit, M., Kangang, P., Grégoire, M., Duchene, S., et al., 2012. Mineralogy, geochemistry and petrogenesis of the recent magmatic formations from Mbengwi, a continental sector of the Cameroon Volcanic Line (CVL), Central Africa. *Mineralogy and Petrology* 106, 217–242.
- Morra, V., Secchi, F.A.G., Assorgia, A., 1994. Petrogenetic significance of peralkaline rocks from Cenozoic calc-alkaline volcanism from SW Sardinia, Italy. *Chemical Geology* 118, 109–142.
- Niu, Y., Batiza, R., 1997. Trace element evidence from seamounts for recycled oceanic crust in the eastern Pacific mantle. *Earth and Planetary Science Letters* 148, 471–483.
- Niu, Y., Collerson, K.D., Batiza, R., Wendt, J.I., Regelous, M., 1999. The origin of E-Type MORB at ridges far from mantle plumes: the East Pacific Rise at 11°20'. *Journal of Geophysical Research* 104, 7067–7087.
- Niu, Y., Hékinian, R., 1997. Basaltic liquids and harzburgitic residues in the Garrett Transform: a case study at fast-spreading ridges. *Earth and Planetary Science Letters* 146, 243–258.
- Niu, Y., O'Hara, M.J., 2009. MORB mantle hosts the missing Eu (Sr, Nb, Ta and Ti) in the continental crust: new perspectives on crustal growth, crust–mantle differentiation and chemical structure of oceanic upper mantle. *Lithos* 112, 1–17.
- Niu, Y., O'Hara, M.J., 2003. The origin of ocean island basalts (OIB): a new perspective from petrology, geochemistry and mineral physics considerations. *Journal of Geophysical Research* 108, 1–19 (ECV5).
- Niu, Y., Waggoner, G., Sinton, J.M., Mahoney, J.J., 1996. Mantle source heterogeneity and melting processes beneath seafloor spreading centers: the East Pacific Rise 18°–19°S. *Journal of Geophysical Research* 101, 711–733.
- Niu, Y., Zhao, Z., Zhu, D., Mo, X., 2013. Continental collision zones are primary sites for net continental crust growth—a testable hypothesis. *Earth-Science Reviews* 127, 96–110.
- Parker, D.F., Ren, M., Adams, D.T., Tsai, H., Long, L.E., 2012. Mid-Tertiary magmatism in western Big Bend National Park, Texas, U.S.A.: evolution of basaltic source regions and generation of peralkaline rhyolite. *Lithos* 144, 161–176.
- Peccerillo, A., Barberio, M.R., Yirgu, G., Ayalew, D., Barbieri, M., Wu, T.W., 2003. Relationships between mafic and peralkaline silicic magmatism in continental rift settings: a petrological, geochemical and isotopic study of the Gedemsa volcano, central Ethiopian Rift. *Journal of Petrology* 44, 2003–2032.
- Peccerillo, A., Donati, C., Santo, A.P., Orlando, A., Yirgu, G., Ayalew, D., 2007. Petrogenesis of silicic peralkaline rocks in the Ethiopian rift: geochemical evidence and volcanology implications. *Journal of African Earth Sciences* 48, 161–173.
- Regelous, M., Niu, Y., Wendt, J.I., Batizab, R., Greiga, A., Collerson, K.D., 1999. Variations in the geochemistry of magmatism on the East Pacific Rise at 10°30'N since 800 ka. *Earth and Planetary Science Letters* 168, 45–63.
- Ren, M., Omenda, P.A., Anthony, E.Y., White, J.C., Macdonald, R., Berley, D.K., 2006. Application of the QUILF thermobarometer to the peralkaline trachyte and pantellerites of the Eburi volcanic complex, East Africa Rift, Kenya. *Lithos* 91, 109–124.
- Renna, M.R., Tribuzio, R., Braga, R., 2013. Petrogenesis relationships between peralkaline rhyolite dykes and mafic rocks in the post-Variscan gabbroic complex from Bocca di Tenda (Northern Corsica, France). *Contribution to Mineralogy and Petrology* 165 pp. 1073–1085.
- Ronga, F., Lustrino, M., Marzoli, A., Melluso, L., 2010. Petrogenesis of a basalt–comendite–pantellerite rock suite: the Bosetti Volcanic Complex (Main Ethiopian Rift). *Mineralogy and Petrology* 98, 227–243.
- Rooney, T.O., Hart, W.K., Hall, C.M., Ayalew, D., Chiorso, M.S., Hidalgo, P., et al., 2012. Peralkaline magma evolution and the tephra record in the Ethiopian Rift. *Contribution to Mineralogy and Petrology* 164 pp. 407–426.
- Rudnick, R.L., Gao, S., 2003. Composition of the continental crust. In: Holland, H.D., Turekian, K.K. (Eds.), *Treatise on Geochemistry* 3. Elsevier-Pergamon, Oxford, pp. 1–64.
- Saillet, B., Macdonald, R., 2003. Experimental constraints on the relationships between peralkaline rhyolites of the Kenya Rift Valley. *Journal of Petrology* 44, 1867–1894.
- Stevens, N.C., 1989. Glass house. In: Johnson, R.W. (Ed.), *Intraplate Volcanism in Eastern Australia and New Zealand*. Cambridge University Press, Cambridge, pp. 109–110.
- Sui, Q., Wang, Q., Zhu, D., Zhao, Z., Chen, Y., Santosh, M., et al., 2013. Compositional diversity of ca. 110 magmatism in the northern Lhasa Terrane, Tibet: implications for the magmatic origin and crustal growth in a continent–continent collision zone. *Lithos* 168–169, 144–159.
- Sun, S.S., McDonough, W.F., 1989. Chemical and isotopic systematics in ocean basalt: implications for mantle composition and processes. *Geological Society* 42. Special Publications, London, pp. 313–345.
- Sutherland, F.L., Graham, I.T., Meffre, S., Zwingmann, H., Pogson, R.E., 2012. Passive-margin prolonged volcanism, East Australian Plate: outbursts, progressions plate controls and suggested causes. *Australian Journal of Earth Sciences* 59, 983–1005.
- Wei, H.Q., Wang, Y., Jin, J., 2007. Timescale and evolution of the intracontinental Tianchi volcanic shield and ignimbrite-forming eruption, Changbaishan, Northeast China. *Lithos* 96, 315–324.
- Wellman, P., 1989. Upper mantle, crust, and geophysical volcanology of eastern Australia. In: Johnson, R.W. (Ed.), *Intraplate Volcanism in Eastern Australia and New Zealand*. Cambridge University Press, Cambridge, pp. 29–38.
- Wellman, P., McDougall, I., 1974. Cainozoic igneous activity in eastern Australia. *Tectonophysics* 23, 49–65.
- White, J.C., Benker, S.C., Ren, M., Urbanczyk, K.M., Corrck, D.W., 2006. Petrogenesis and tectonic setting of peralkaline Pine Canyon caldera, Trans-Pecos Texas, USA. *Lithos* 91, 74–94.
- White, J.C., Espejel-Garcia, V.V., Anthony, E.Y., Omenda, P., 2012. Open system evolution of peralkaline trachyte and phonelite from the Suswa volcano, Kenya rift. *Lithos* 152, 84–104.
- White, J.C., Parker, D.F., Ren, M., 2009. The origin of trachyte and pantellerite from Pantelleria, Italy: insights from major element, trace element, and thermodynamic modeling. *Journal of Volcanology and Geothermal Research* 179, 33–55.
- Zou, H., Fan, Q., Zhang, H., 2010. Rapid development of the great Millennium eruption of Changbaishan (Tianchi) volcano, China/North Korea: evidence from U-Th zircon dating. *Lithos* 119, 289–296.